Chapter 5

Analysis

In experiment E02-013 the electric form factor of the neutron was measured at four kinematic points. Three of these kinematic pointsare presented in this thesis. The analysis procedure, excluding the initial decoding and analysis steps, is shown in flow charts in Figures 5.1, 5.2, and 5.3. The initial decoding and analysis passes provide the electron arm physics information, as described in section 4.7, in addition to neutron arm cluster information. The first step of this procedure is the event based filtering, as described in Table 5.1, which uses the time-of-flight of the electron, momentum, invariant mass of the recoiling hadron, and transferred momentum vectors which were already calculated from the electron arm (in section 5.1 and 5.2) information to select hadron event candidates. Next, hadrons are identified using the transferred momentum vectors and the constructed time-of-flight of the hadron, which is discussed in more detail in section 5.3. A charge is assigned to these hadrons as described in section 5.4. Next, various dilutions of the asymmetry (section 3.3), and corrections to it, are described and calculated in section 5.5. The neutron physical asymmetry determined from the neutral quasi-elastic events is then calculated in section 5.6, using the Table 5.6. In this section preliminary results for the electric form factor are also presented with corrections. The final state interaction corrections which will be included in the final value of G_E^n are discussed

in section 5.7. Discussion of error propagation can be found in Appendix B.

Electron event selection in the Big Bite spectrometer was achieved by means of the shower detector and scattering angle. Selection of events from within the target and by a coarse cut on transferred momentum were made using the multi-wire drift chamber (MWDC). Hadron identification was achieved using the location and time of the hit in the neutron detectors, and by using the veto detectors to differentiate the protons from the neutrons. Finally missing mass, missing momentum, and invariant mass were used to select the quasi-elastic process.

5.1 Event filtering and scintillator timing

The total shower detector, as described in section 4.5.2, is divided into two parts, called the shower and the pre-shower, separated by a plane of scintillator detectors. Using only the pre-shower amplitude, pions and electrons could be identified and clearly differentiated, (as shown in Figure 5.4). Obviously, for any selection based on preshower energy which doesn't remove an unreasonable portion of electrons, some portion of pions will still exist in the selected sample. These pions will create a dilution of the (e,e'h) interaction. An emperical study was done to determine the contamination of the neutral hadron candidate sample by $(ep, e'\pi^0 n)$ events. This contamination was shown to be less than 2% [2].

While the total shower was the hardware trigger for the electron arm, the time based on the calorimeter alone would not provide the needed resolution for the event. This function is provided by the plane of scintillators directly behind the

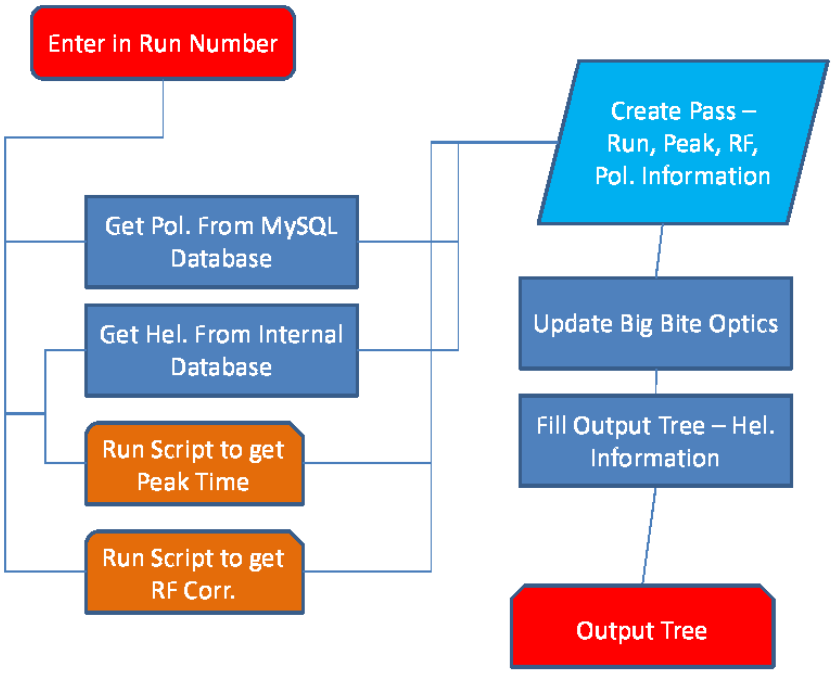

Figure 5.1: The flowchart for the analysis. This is after the preliminary replay of events that is described in section 4.7. The resulting ROOT files contain the subset of events necessary to undertake the remaining analysis, also assigns charge, and identifies quasi-elastic event candidates. Two separate scripts are ran as part of this process for each run before this post processing. This is to determine the RF correction (see section 5.5.3) and the hadron time-of-flight.

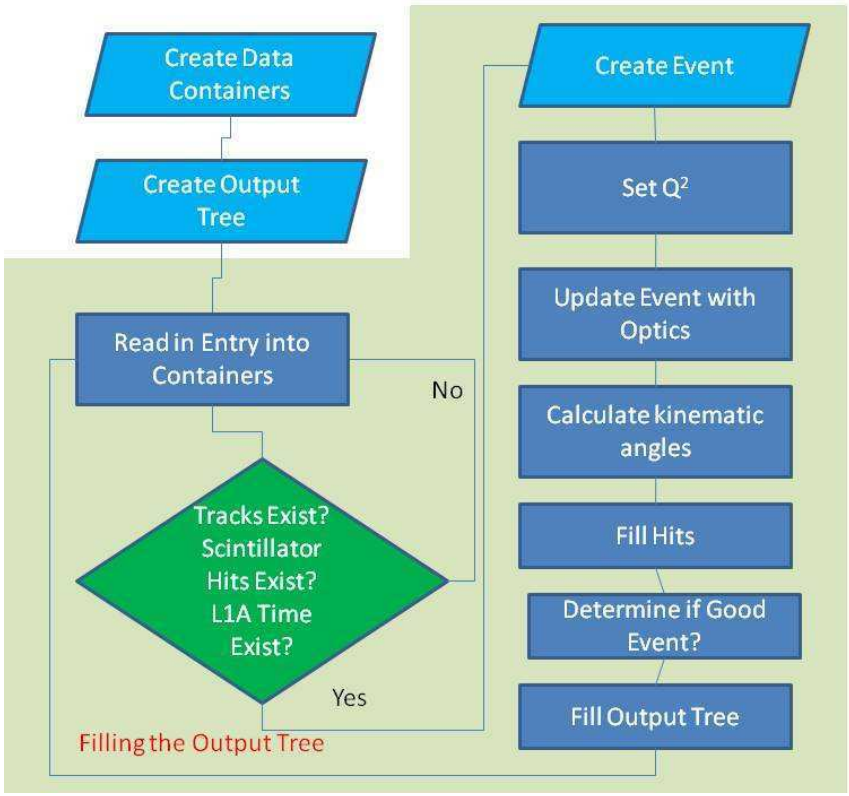

Figure 5.2: Flowchart for the event processing. Events in the analysis are ignored if no tracks or Big Bite scintillator hits exist, or if the event does not have a well defined trigger time as demonstrated by the existence of the Level 1 Accept (L1A) Time. The optics can be updated here if necessary, and the kinematics of the event are calculated to ease post processing. All event cuts are detailed in Table 5.1.

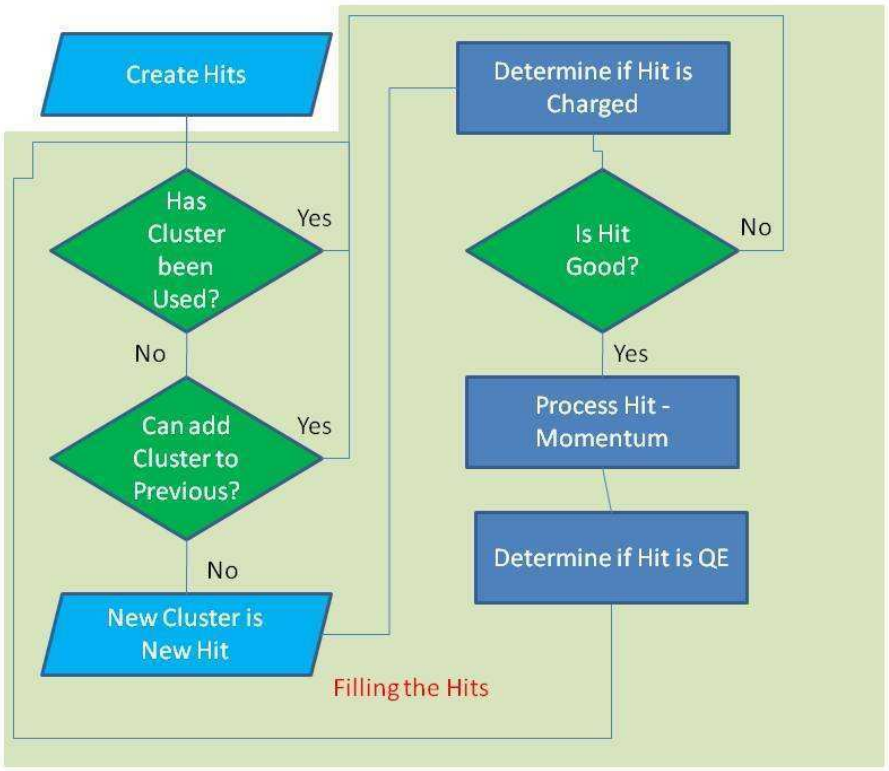

Figure 5.3: Flowchart associating clusters, both with each other and as quasi-elastic event candidates. Some clusters should be associated together, where some neutron detector did not fire to make the cluster continuous. Charged candidates are identified, and momentum is calculated for the hit.

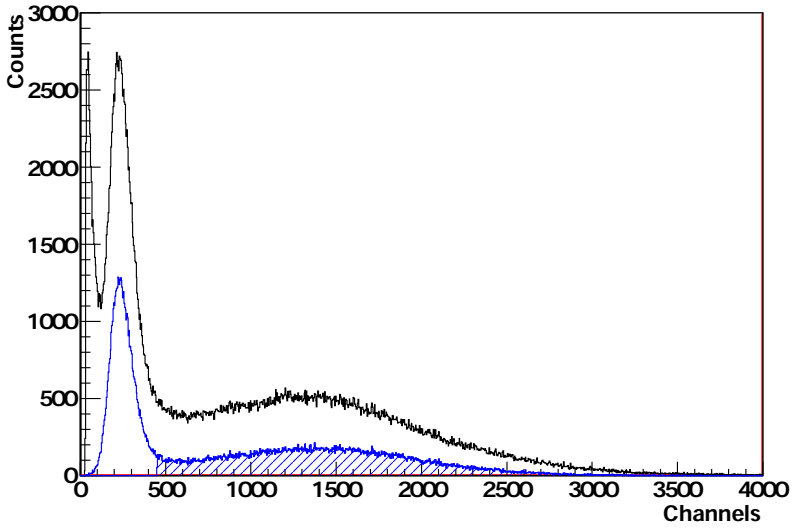

Figure 5.4: Amplitude distribution for all events showing pions and electrons in Big Bite. In blue is the distribution after cuts have been applied to remove events which are lacking the information needed for analysis, shaded is the region selected. See Table 5.1 for cuts, in black is all events and in blue is with just the "sanity" cuts applied. This distribution is for $Q^2 = 3.5$ GeV^2.

pre-shower, which served as the primary time reference for both the electron and neutron arms. The path length for the electron was emperically determined using the optics with respect to this plane. This reference time was corrected for the variations in path length coming from differences in vertex location and corrections for vertical and horizontal position in the scintillator stack.

The time of the event within the electron arm, t_e, can be presented as the time in the scintillator t_s, with corrections for the vertical path length t_x, the horizontal path length t_y, and the difference between the scintillator plane and the wire chamber t_c.

$$t_e = t_s - t_x - t_y - t_c \tag{5.1}$$

$$t_x = \frac{1}{c} 1.2 |P_{x,BB} + 0.25| \tag{5.2}$$

$$t_y = \frac{1}{c} \frac{[2.2532 \sin(-\theta_{BB}) + Y_{BB} \cos(-\theta_{BB})]}{\sin[\tan^{-1}(P_{y,BB}) - \theta_{BB}]} - 2.2 \tag{5.3}$$

$$t_c = \frac{1}{c} \left(L_{D2S} (1 + P_{x,BB}^2 + P_{y,BB}^2 \right)^2 \tag{5.4}$$

Here, $L_{D2S} = 0.95$ m is the time from the detector to the scintillator, $P_{x,BB}$ is the track slope $\tan\Theta = \frac{dx}{dz}$ in Big Bite detector coordinates, $P_{y,BB}$ is the track slope $\tan\Phi = \frac{dy}{dz}$ in Big Bite detector coordinates, Y_{BB} is the reconstructed horizontal position vector y in Big Bite detector coordinates, and $\theta_{BB} = 51.59$ degrees is the central angle at which the detector was placed for the Q^2 of 1.7, 2.5, and 3.5 GeV^2. The other constants were empirically determined using the optics data.

5.2 Electron parameters

Quasi-elastic (from ^{3}He) and elastic events (from hydrogen) were selected using the momentum of the electron as measured by the Big Bite spectrometer in addition to deposited energy in the preshower (see Figure 5.5). Additional event selection was performed by removing events that were reconstructed to start from outside of the target (see Figure 5.7), or that travelled through a region of Big Bite where the magnetic field is not well understood (see Figure 5.6). Among the quantities computed from the identified electron tracks are the invariant mass of the hadron, the transferred momentum of the virtual photon, the electron momentum, and the electron scattering angle.

The transferred momentum, $\vec{q}$, calculated from the beam energy and scattered electron momentum, was used in the identification of quasi-elastic hits within the neutron arm. The transferred momentum is entirely independent of the neutron arm time-of-flight. The parallel and perpendicular components of transferred momentum with respect to the hadron momentum vector can be defined as

$$q_{\parallel} = \vec{q} \cdot \hat{p}_h \ , \tag{5.5}$$

$$q_{\perp} = \vec{q} \times \hat{p}_h \ . \tag{5.6}$$

Here $\hat{p}_h$ is the unit vector of the hadron momentum as determined by the neutron arm. This is determined purely from the hit location (x, y, and z) in the neutron arm, and is independent of time-of-flight.

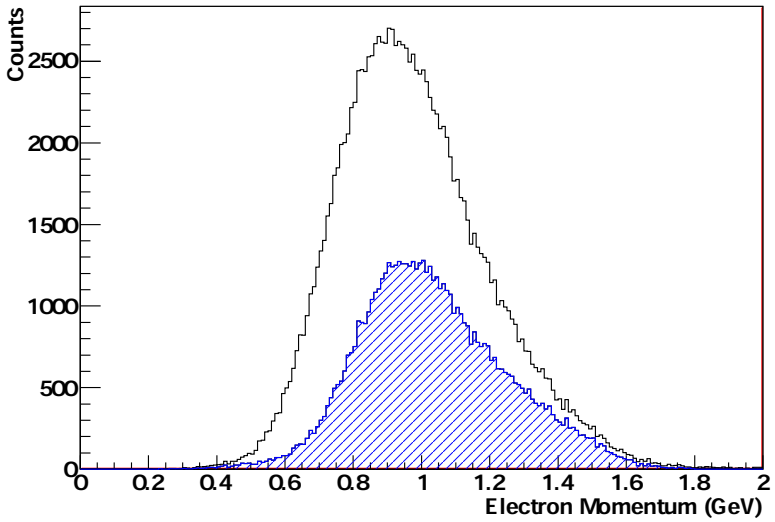

Figure 5.5: Electron momentum for all tracks in Big Bite. In blue are just those tracks for which the preshower energy is greater than 450 channels, shaded is the selected momentum. See Table 5.1 for cuts, in black is all events and in blue is with the "sanity" and pre-shower energy cuts applied. This distribution is for $Q^2 = 3.5$ GeV^2.

The invariant mass of the hadron is

$$W^2 = M_N^2 - Q^2 + \frac{2\vec{p_e} \cdot \vec{q}}{M_N} \ . \tag{5.7}$$

Here M_N is the nucleon mass, Q^2 is the transferred four-momentum squared (see section 2.2), and $\vec{p_e}$ is the electron momentum.

The invariant mass and perpendicular transferred momentum ($q_\perp$) are the two time-of-flight independent variables which are used for quasi-elastic event selection. The selection of quasi-elastic events are shown for $Q^2 = 2.5$ GeV^2 in Figure 5.8(a) and 5.9(a). Both of these figures include fidicual cuts in the neutron arm. The final quasi-elastic neutral candidates selection for kinematic 2 as well as the overall spectrum is presented in perpendicular transferred momentum is presented in Figure

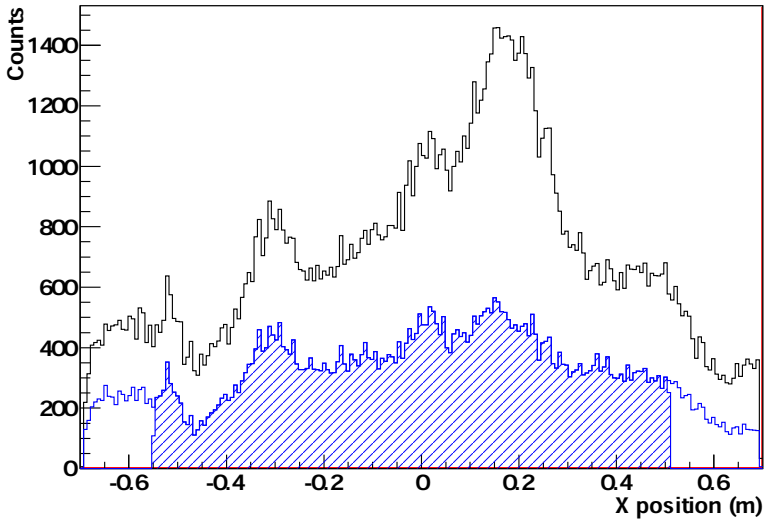

Figure 5.6: X position (m) within the Big Bite scintillator detector. This is for before cuts (black), after electron and sanity cuts (blue), with the selected region of X shaded. Variation is due to the lack of calibration for the total shower in the Big Bite detector. See Table 5.1 for cuts, in black is all events and in blue is with the "sanity", pre-shower energy, and electron momentum cuts applied. This distribution is for $Q^2 = 3.5$ GeV^2.

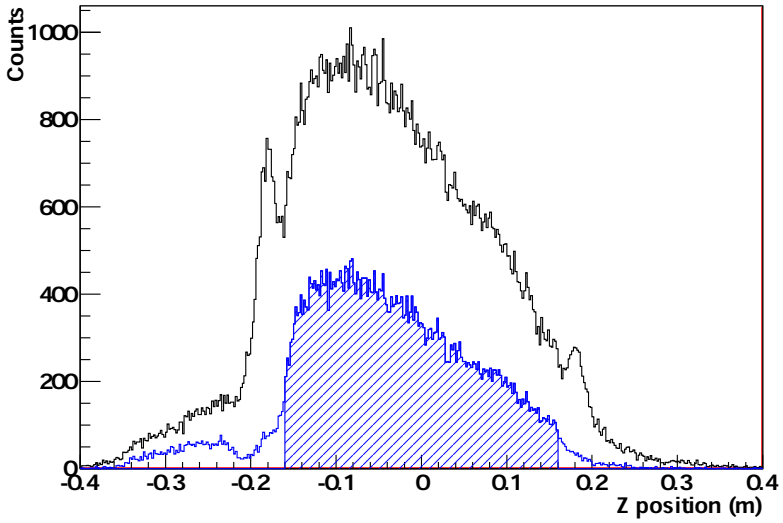

Figure 5.7: Vertex, this shows the target z position reconstructed by the Big Bite wire chambers for all events with tracks (black). In blue is after cuts on particle ID. Shaded is the region selected as being within the target. See Table 5.1 for cuts, in black is all events and in blue is with the "sanity", pre-shower energy, Big Bite fidicual, and electron momentum cuts applied. This distribution is for $Q^2 = 3.5$ GeV^2.

name	$Q^2 = 2.5$ GeV^2	$Q^2 = 3.5$ GeV^2	$Q^2 = 1.7$ GeV^2
W (GeV)	$\|W - 0.95\| < 0.6$	$\|W - 0.95\| < 0.6$	$\|W - 0.95\| < 0.6$
E. E. (MeV)	$E_{ps} > 450$	$E_{ps} > 450$	$E_{ps} > 450$
E. Mom.(GeV)	$\|p_e - 1.1\| < 0.9$	$\|p_e - 1.1\| < 0.9$	$\|p_e - 1.1\| < 0.9$
Vertex (m)	$\|V_{tgt}\| < 0.16$	$\|V_{tgt}\| < 0.16$	$\|V_{tgt}\| < 0.16$
X Fid. (m)	$-0.4 < X_{BB} < 0.45$	$-0.4 < X_{BB} < 0.45$	$-0.4 < X_{BB} < 0.45$
Sanity 1	$N_{Tracks} > 0$	$N_{Tracks} > 0$	$N_{Tracks} > 0$
Sanity 2	$N_{Paddles} \geq 0$	$N_{Paddles} \geq 0$	$N_{Paddles} \geq 0$
Sanity 3 (Ch)	$t_{L1A} < 4000$	$t_{L1A} < 4000$	$t_{L1A} < 4000$
Sanity 4	$N_{Type3} > 0$	$N_{Type3} > 0$	$N_{Type3} > 0$
Negative	$P_{x,BB} - 0.3X_{BB} < 0$	$P_{x,BB} - 0.3X_{BB} < 0$	$P_{x,BB} - 0.3X_{BB} < 0$

Table 5.1: A table of the initial event selection for analysis. Sanity cut 1 is the requirement that Big Bite has a track, Sanity cut 2 is the requirement that at least one scintillator paddle in Big Bite has an event, Sanity cut 3 is that the coincidence time (L1A) was recorded. Sanity cut 4 is the requirment that there is a coincidence event. Negative is a requirement that only negative particles in the drift chambers can be considered as electrons.

5.11(a). The expected invariant mass is about 0.94 GeV, the mass of a nucleon.

5.3 Hadron identification

Once electron events are selected and the invariant mass and the direction and magnitude of $\vec{q}$ are determined from information from the Big Bite spectrometer, the neutron arm is used to determine the three-momentum and charge of the hadron. Hits in the neutron arm were joined together into clusters as described in Appendix A.4.1. Typically, multiple bars recorded hits in the same event in the neutron apparatus due to particles with high energy traveling deep into the neutron apparatus, and to the segmented nature of the neutron apparatus.

The time of the counter with the earliest hit (of those nearby in time and space) was used as the time of the cluster. This time, the time of the electron

in the Big Bite scintillator, and the relevant path lengths allow the calculation of the momentum of the particle, assuming it is a hadron. Only those hits where the calculated momentum is less than c are included in the analysis.

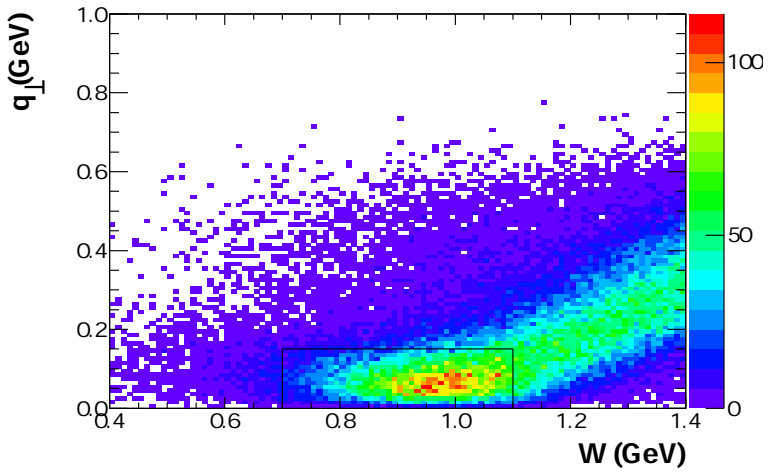

(a) $Q^2 = 2.5$ GeV^2 $q_\perp$

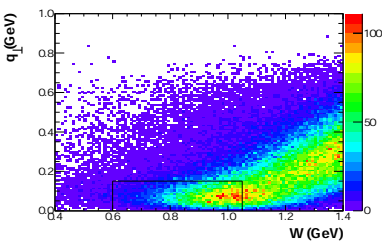

(b) $Q^2 = 3.5$ GeV^2 $q_\perp$

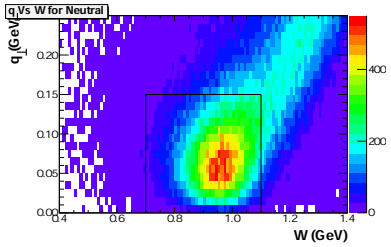

(c) $Q^2 = 1.7$ GeV^2 $q_\perp$

Figure 5.8: $q_\perp$ versus W for neutral particles in the various kinematics. Shown is the selection of quasi-elastic events in the red square. As shown, at higher Q^2 the inelastic tail becomes stronger.

The clusters were combined if they were nearby in time and space. The time and position of only the first hits were used to determine whether the later cluster(s) should be considered part of the earlier cluster. Multiple clusters in a single event were considered as a single cluster if δX (vertical position) and δZ (depth) were within 0.4 m, and δY (horizontal position) was within 0.2 m. Additionally, the time

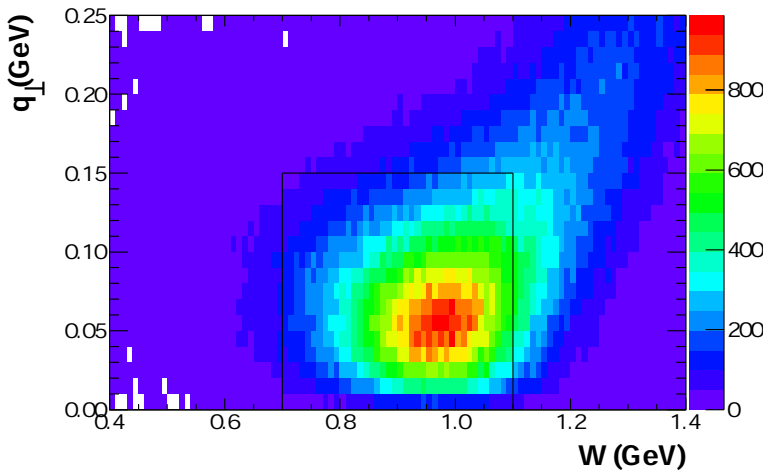

(a) $Q^2 = 2.5$ GeV^2 $q_\perp$

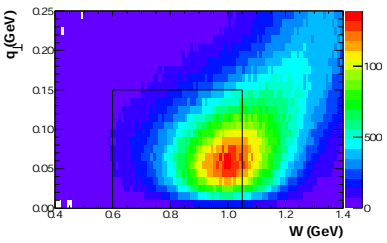

(b) $Q^2 = 3.5$ GeV^2 $q_\perp$

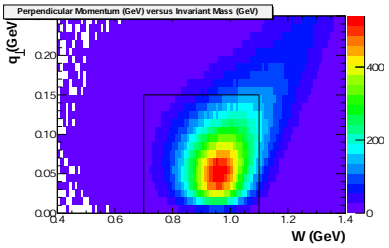

(c) $Q^2 = 1.7$ GeV^2 $q_\perp$

Figure 5.9: $q_\perp$ versus W for charged particles in the various kinematics. In the red box is the selection of quasi-elastic events.

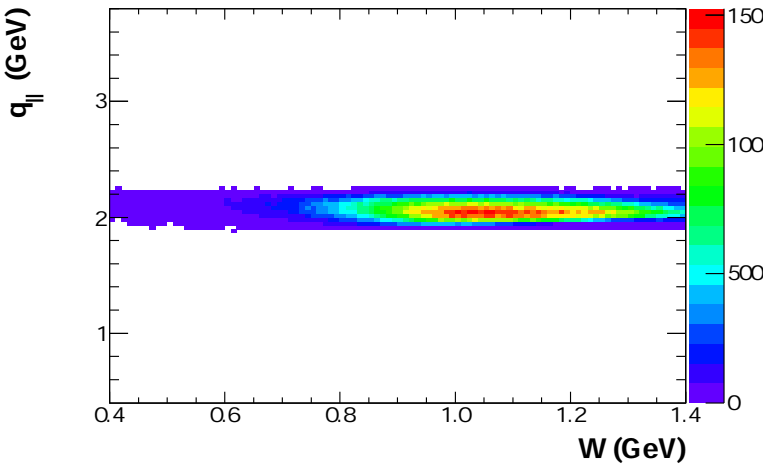

(a) $Q^2 = 2.5$ GeV^2 $q_{\|}$

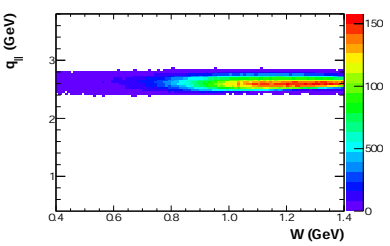

(b) $Q^2 = 3.5$ GeV^2 $q_{\|}$

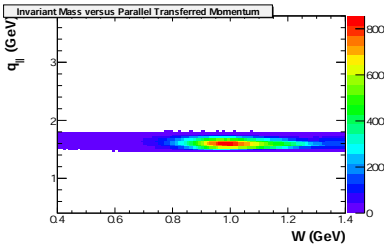

(c) $Q^2 = 1.7$ GeV^2 $q_{\|}$

Figure 5.10: $q_{\|}$ versus W for charged particles in kinematic 3. ? - ? In the conversion section or the ND section ? - ?

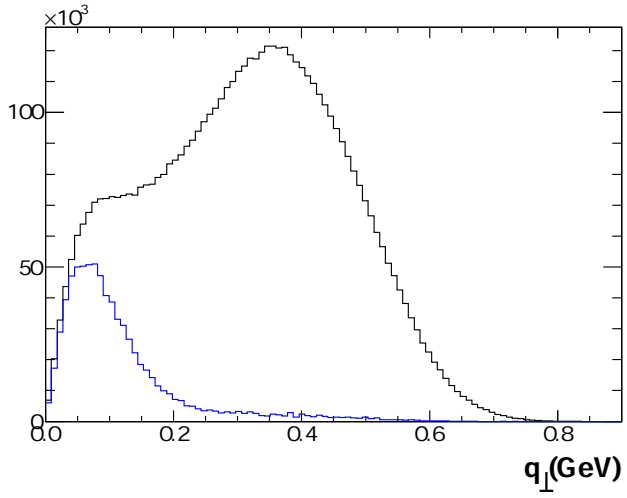

(a) $Q^2 = 2.5$ GeV^2 $q_\perp$

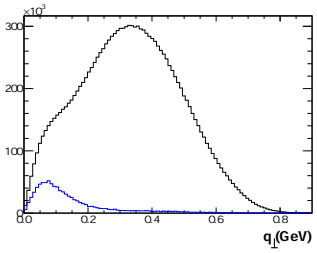

(b) $Q^2 = 3.5$ GeV^2 $q_\perp$

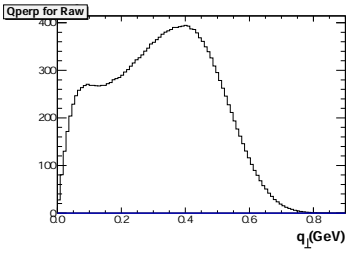

(c) $Q^2 = 1.7$ GeV^2 $q_\perp$

Figure 5.11: Distribution of $q_\perp$ in the various kinematics. Shown in blue is the neutral spectrum, in black is the total spectrum (That passed the event based selection). The majority of neutral quasi-elastic events fall under 0.15 GeV.

difference had to be within 10 ns. See Appendix A for more discussion of clusters and neutron arm software.

The expected time for hadron event within the neutron arm T_h is given by

$$T_h = \frac{\sqrt{L_{NA}^2 + Z_{tgt}^2 - 2L_{NA}Z_{tgt}\hat{p}_h \cdot \hat{z}}}{\frac{q}{\sqrt{m_h^2+q^2}}} \ . \tag{5.8}$$

Here L_{NA} is the path measured from the center of the target to the neutron arm hit, Z_{tgt} is position of the interaction in the target as reconstructed by Big Bite, $\vec{p}_h$ is the hadron momentum vector (in the laboratory coordinate system). Since at this point the charge of the hadron is unknown, its mass is nominally set to the nucleon mass $m_N = 0.939$ GeV.

This is compared to the actual time-of-flight which is constructed from the measured location of the time-of-flight peak measured using the neutron arm and Big Bite scintillators. This actual time is constructed as

$$T_{TOF} = t_{NA} - t_e + t_{rf} + t_{L1A} - t_{peak} \ . \tag{5.9}$$

Here, the t_{NA} is the time measured in the neutron arm, t_{rf} is the correction that can be done using the beam information (to be discussed in section 5.5.3), t_{L1A} is the level 1 accept time, and t_{peak} is the peak location in the total time-of-flight spectrum. To select quasi-elastic events, the expected time-of-flight is compared to the actual time-of-flight, giving ΔT. The time-of-flight spectrum for total events and quasi-elastic neutral candidates in kinematic 2 is shown in Figure 5.12(a).

From the time-of-flight, the hadron velocity, β, and momentum, p_h, can be

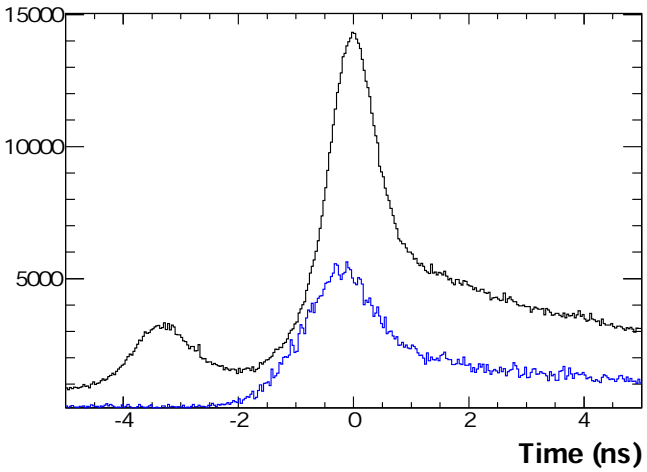

(a) $Q^2 = 2.5$ GeV^2 time

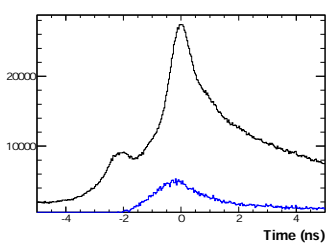

(b) $Q^2 = 3.5$ GeV^2 time

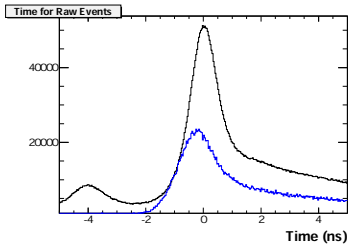

(c) $Q^2 = 1.7$ GeV^2 time

Figure 5.12: ΔT (ns) for the various kinematics. In blue is the neutral time-of-flight spectrum, in black is the total time-of-flight spectrum. The photon peak is shown at ≈ -3ns. Quasi-elastic events are selected with time between -1 and 1 ns.

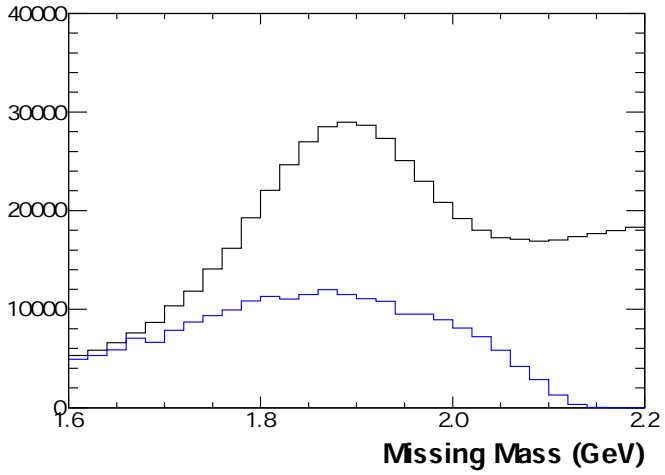

(a) $Q^2 = 2.5$ GeV^2 missing mass

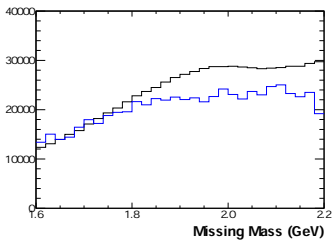

(b) $Q^2 = 3.5$ GeV^2 missing mass

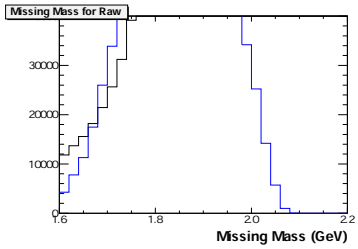

(c) $Q^2 = 1.7$ GeV^2 missing mass

Figure 5.13: Missing mass (GeV) for the various kinematics. In blue is the neutral scaled up by a factor of 20 for $Q^2 = 3.5$ GeV^2 and 10 for $Q^2 = 2.5$ GeV^2, in black is the total spectrum.

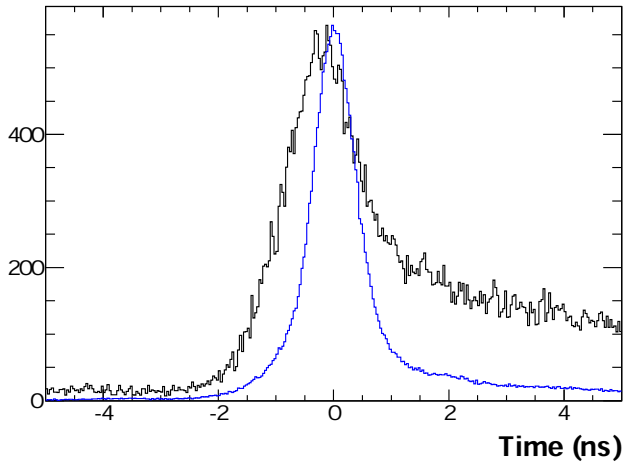

(a) $Q^2 = 2.5$ GeV^2 time

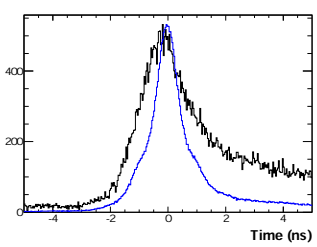

(b) $Q^2 = 3.5$ GeV^2 time

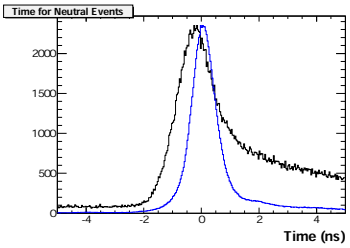

(c) $Q^2 = 1.7$ GeV^2 time

Figure 5.14: ΔT (ns) for the various kinematics. In blue is the charged time-of-flight spectrum, in blue is the charged time-of-flight spectrum. The charged spectrum is scaled down to the neutral spectrum.

constructed (all in laboratory coordinates):

$$\beta = \frac{L_{NA}^2 + V_{tgt}^2 - 2L_{NA}V_{tgt}\hat{p}_h \cdot \hat{z}}{cT_{TOF}} \ , \tag{5.10}$$

$$p_h = \frac{m_h}{\sqrt{1-\beta^2}} \ . \tag{5.11}$$

Also calculated is the unit vector relating this hit and the central location in the target. Additionally, the perpendicular and parallel momenta can be calculated:

$$p_{h,\parallel} = \vec{p}_h \cdot \hat{q} \tag{5.12}$$

$$p_{h,\perp} = \vec{p}_h \times \hat{q} \ . \tag{5.13}$$

An additional quantity used to select quasi-elastic events which is dependent on hadron identification is the missing mass. This is defined as

$$M_{miss}^2 = (\mathbf{P}_i + \mathbf{q} - \mathbf{p}_h)^2 = (E_{He} + E_q - E_p)^2 - (\vec{q} - \vec{p}_h)^2 \ , \tag{5.14}$$

where $\mathbf{P}_i$ is the initial ^{3}He momentum four-vector, $\mathbf{q}$ is the transferred momentum four-vector and $\mathbf{p}_h$ is the nucleon four-vector.

The selection of quasi-elastic neutral events using time, invariant mass, and $q_\perp$ is demonstrated in Figures 5.15(a) and 5.16(a). The inelastic contribution becomes larger at higher Q^2 and so more aggressive cuts in invariant mass must be used.

5.4 Identification of the hadron charge

While a particle can be determined to be a recoil hadron candidate by hit location and time-of-flight, it is not easy to differentiate between protons and neutrons using only this information from within the neutron counters. For the purpose

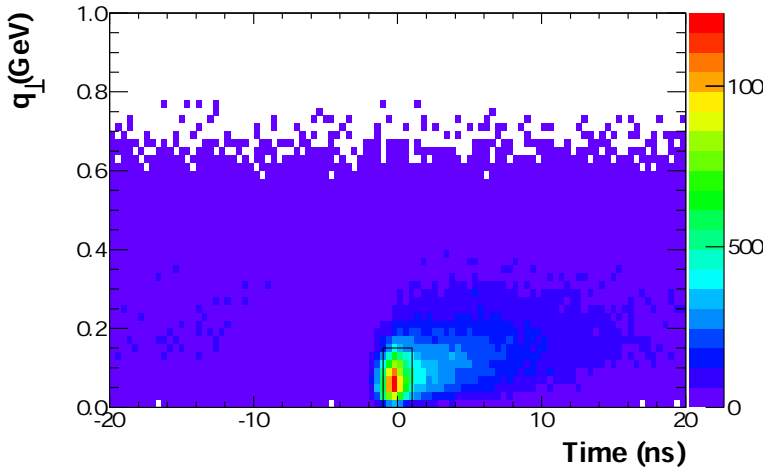

(a) $Q^2 = 2.5$ GeV^2 time versus $q_\perp$

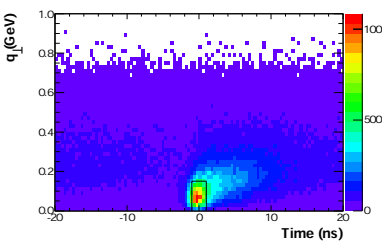

(b) $Q^2 = 3.5$ GeV^2 time versus $q_\perp$

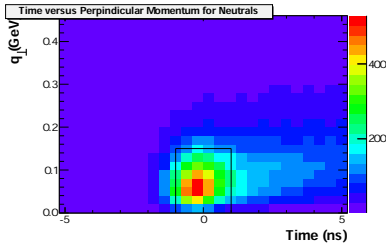

(c) $Q^2 = 1.7$ GeV^2 time versus $q_\perp$

Figure 5.15: Shown in these figures is the time versus $q_\perp$ for various kinematics. Also shown is the box showing which cuts were used for identifying quasi-elastic clusters within the neutron arm. As is shown, the ability to select quasi-elastic clusters is much better for the lower kinematics.

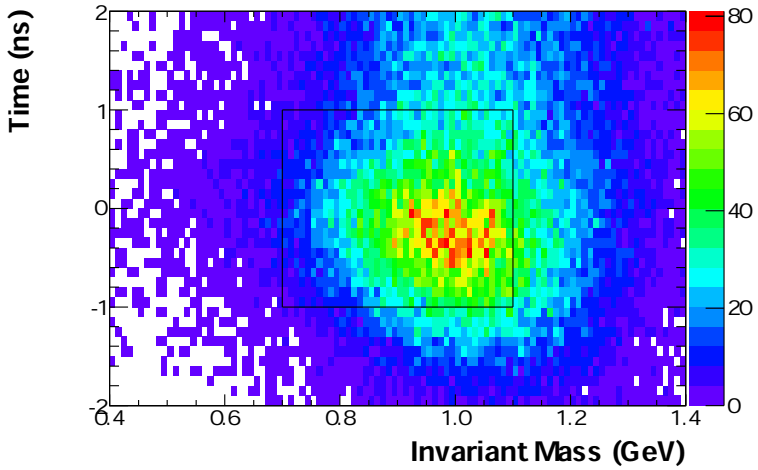

(a) $Q^2 = 2.5$ GeV^2 time versus invariant mass

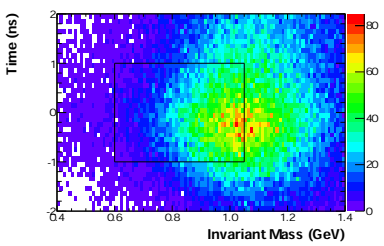

(b) $Q^2 = 3.5$ GeV^2 time versus invariant mass

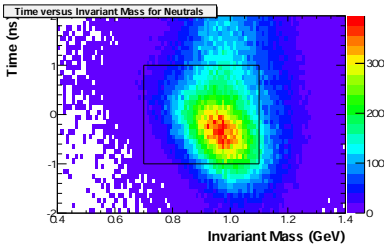

(c) $Q^2 = 1.7$ GeV^2 time versus invariant mass

Figure 5.16: Shown in these figures is the time versus invariant mass for various kinematics. Also shown is the box showing which cuts were used for identifying quasi-elastic clusters within the neutron arm. As is shown, the ability to select quasi-elastic clusters is much better for the lower kinematics.

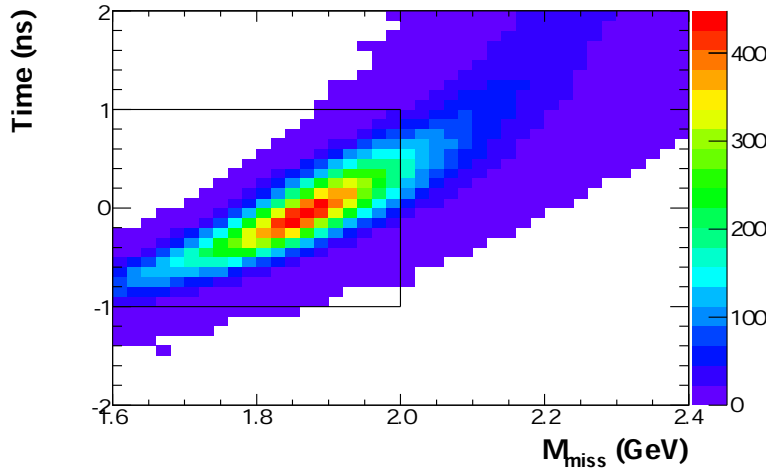

(a) $Q^2 = 2.5$ GeV^2 invariant mass versus missing mass

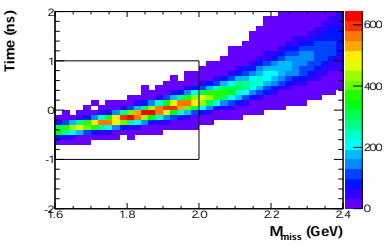

(b) $Q^2 = 3.5$ GeV^2 invariant mass versus missing mass

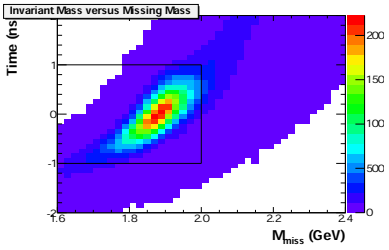

(c) $Q^2 = 1.7$ GeV^2 invariant mass versus missing mass

Figure 5.17: Shown in these figures is the time versus missing mass for various kinematics. Also shown is the box showing which cuts were used for identifying quasi-elastic clusters within the neutron arm. As is shown, the ability to select quasi-elastic clusters is much better for the lower kinematics.

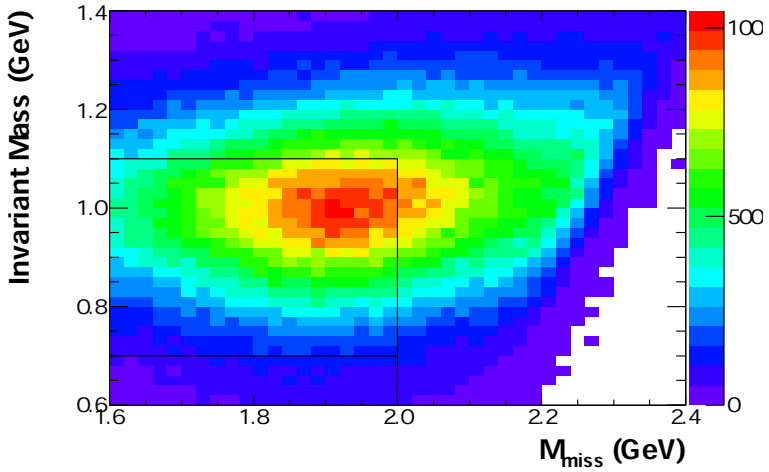

(a) $Q^2 = 2.5$ GeV^2 invariant mass versus missing mass

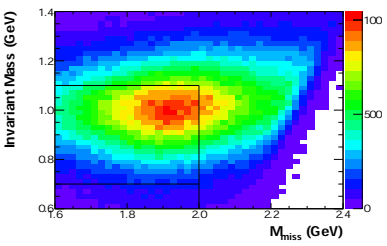

(b) $Q^2 = 3.5$ GeV^2 invariant mass versus missing mass

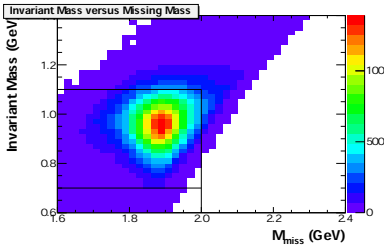

(c) $Q^2 = 1.7$ GeV^2 invariant mass versus missing mass

Figure 5.18: Shown in these figures is the invariant mass versus missing mass for various kinematics. Also shown is the box showing which cuts were used for identifying quasi-elastic clusters within the neutron arm. As is shown, the ability to select quasi-elastic clusters is much better for the lower kinematics.

of charge identification, two layers of veto counters were positioned in front of the neutron counters but behind some of the lead shielding (see section 4.6.1).

The charge of these hadrons was determined by an analysis of hits in the veto in a neighborhood around the hadron hit position in the neutron counters. The veto detectors were segmented vertically similarly to the neutron detectors. Due to scattering in the shielding and detectors, the relevant veto hit position could be greater than a few centimeters away from the identified hadron hit location. The factors used to select relevant veto detectors are listed in Table 5.4.

Determination of whether the hadron is charged or not was accomplished using the time between the neutron bar hit and the veto hit and the segmentation of the detectors. This segmentation defined the x and y position of each veto hit. The individual veto detectors had high rates (1 MHz) and high dead-time (up to 110 ns). This indicates that there exists a large number of possible hits where an earlier accidental hit masked the hit from the quasi-elastic event candidate. For coincident events, the hit in the veto bars varied in veto amplitude in addition to time, the veto amplitude was used in addition to time when selecting veto hits to associate to quasi-elastic events.

While it would be nice to have a detector with uniform neutron detection efficiency, this was not the case for Big Hand. The GLA detectors did not have the resolution to identify quasi-elastic neutrons as the rest of the neutron arm could, and the horizontal edges were not adequently covered by the veto detectors. Two additional cuts, on the neutron arm's x and y fidicual regions were used to select the region of the detector that had a high neutron detection efficiency. This selection is

name	$Q^2 = 2.5$ GeV^2	$Q^2 = 3.5$ GeV^2	$Q^2 = 1.7$ GeV^2
Amplitude	$A_V < 200$	$A_V < 200$	$A_V < 200$
Spatial (m)	$\|X_V - X_C\| < 0.3$	$\|X_V - X_C\| < 0.3$	$\|X_V - X_C\| < 0.3$
Time (ns)	$\|T_V - T_C\| < 10$	$\|T_V - T_C\| < 10$	$\|T_V - T_C\| < 10$
Y1 Cut (m)	$Y_C < 0.076 \& Y_V < 0$	$Y_C < 0.076 \& Y_V < 0$	$Y_C < 0.076 \& Y_V < 0$
Y2 Cut (m)	$Y_C > -0.774 \& Y_V > 0$	$Y_C > -0.774 \& Y_V > 0$	$Y_C > -0.774 \& Y_V > 0$

Table 5.2: A table of selection criteria used to determine which veto hits to consider when doing charge identification. The spatial cuts of Y1, Y2, and X determine which bars are to be included, events were only differentiated by time and amplitude within a veto detector which was within range of the hadron hit. The subscript V signifies veto, while C signifies the cluster in the neutron arm.

shown in Figures 5.19 and 5.20.

The area of the veto used to determine the charge of the hadron is determined by looking at the coincidence between the hadron hit and the veto hit, see Appendix A.5 for more details.

5.5 Dilution of the neutron sample by protons

Between the target and the veto detectors, there were several centimeters of lead and other material [60]. Hadrons that leave the target could be observed as if they were in the other isospin state, through hadronic interactions. This would create a dilution in the neutral candidate sample due to quasi-elastic events still being detected as hadrons, but with the wrong charge. This is especially important in the case of protons observed as neutrons, which creates a significant dilution (see Table 5.5) in the neutron sample. This conversion can be understood, and accounted for, using the ratios of observed protons and neutrons for different targets. The three targets used were hydrogen, which is a single proton, ^{3}He, which is the target of

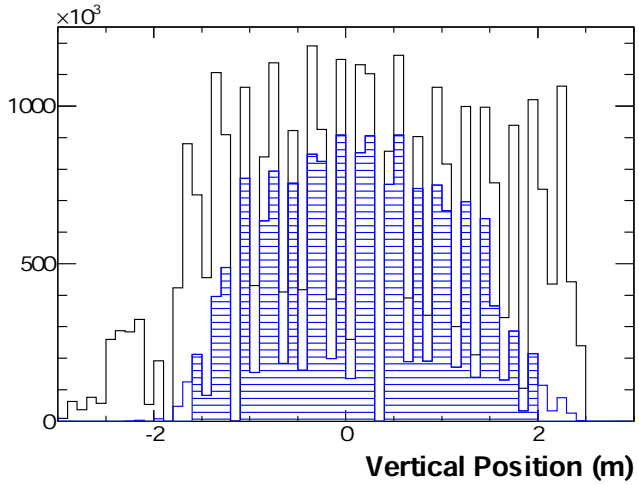

Figure 5.19: Vertical position (m) within the Big Hand detector. This is for before cuts (black), after event selection cuts (blue), with the selected region of x shaded. In the vertical direction the neutron arm was segmented, giving the segmented structure observed. GLA bars are removed, as seen in the most negative region. See Table 5.6 for cuts.This distribution is for $Q^2 = 3.5$ GeV^2.

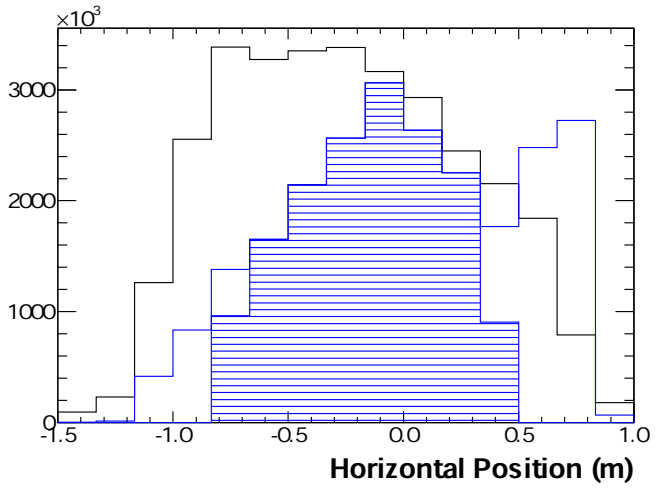

Figure 5.20: Horizontal position (m) within the Big Hand detector. This is for before cuts (black), after event selection cuts (blue), with the selected region of y shaded. In the horizontal direction the neutron arm was not entirely covered by the veto planes, giving the peaks on the two edges. See Table 5.6 for cuts.This distribution is for $Q^2 = 3.5$ GeV^2.

interest, and nitrogen, which has equal numbers of protons and neutrons. These ratios are referred to as R_{tgt},

$$R_{tgt} = \frac{f_n}{f_p} \ . \tag{5.15}$$

Here the subscript tgt stands for target, and is replaced by N for nitrogen, H for hydrogen, and He for ^{3}He. The fraction $f_{p(n)}$ is that of protons(neutrons) to the total number of hadrons.

The purity factor, D_n, is the ratio of observed neutrons to the neutrons knocked out of the target at the interaction point with the electron beam. Similarly, D_p is the ratio of observed protons to those starting from the target. For the observed R_{tgt}, the $f_{p(n)}$ are observed fractions. However, as mentioned, it is possible that interactions between the target and detector can cause a conversion in the observed iso-spin state. To account for this, the ratio can be expressed in terms of mixing coefficients. These provide the numbers of observed $N^{p(n)}$ resulting from an initial target population $N_{p(n)}$. Expressed in this manner

$$R_{tgt} = \frac{N_n^n + N_p^n}{N_p^p + N_n^p} = \frac{\sigma_n \nu_n^n + \frac{Z_{tgt}}{N_{tgt}} \sigma_p \nu_p^n}{\sigma_n \nu_n^p + \frac{Z_{tgt}}{N_{tgt}} \sigma_p \nu_p^p} \ . \tag{5.16}$$

As an example, N_p^n is the number of observed neutrons from initial protons. The above can be presented more compactly as:

$$R_{tgt} = \frac{\frac{\sigma_n}{\sigma_p}\frac{\nu_n^n}{\nu_p^p} + \frac{Z_{tgt}}{N_{tgt}}\frac{\nu_p^n}{\nu_p^p}}{\frac{\sigma_n}{\sigma_p}\frac{\nu_n^p}{\nu_p^p} + \frac{Z_{tgt}}{N_{tgt}}} \ . \tag{5.17}$$

Here $\sigma_{p(n)}$ are the single nucleon cross sections, ν are the mixing coefficients, and $\frac{Z_{tgt}}{N_{tgt}}$ is the ratio of protons to neutrons (unique for each target, and may be dependent on perpendicular and parallel missing momentum) within the target. Obviously

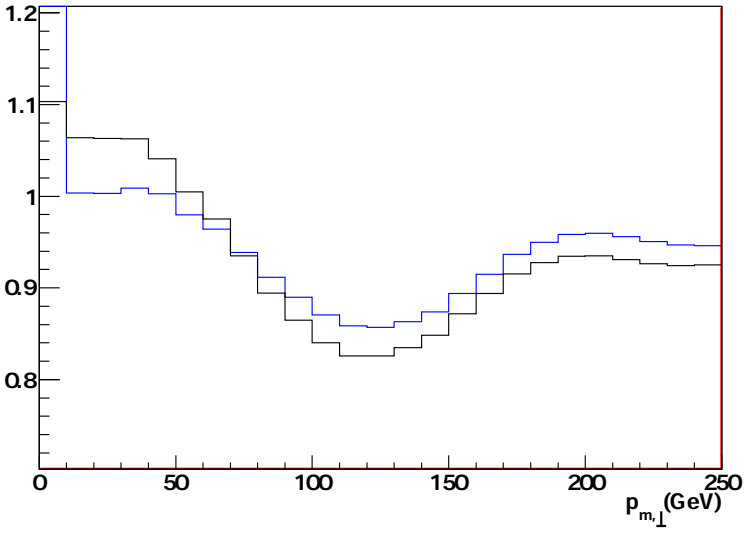

Figure 5.21: Presented is the ratio of protons to neutrons within the target for nitrogen. Shown are two models, one a simple extension to the plane wave impulse approximation (in blue), and the other is a model by Udias (in black). Shown is the ratio for various cuts of $p_\perp$. A cut of 150 MeV was used in this experiment. This is for $Q^2 = 3.5$ GeV^2.

$N_{tgt} = 0$ for hydrogen, $\frac{Z_N}{N_N} \approx 1$ for nitrogen, and $\frac{Z_{He3}}{N_{He3}} \approx 2$ for the ^{3}He. In particular models [][], the ratio was investigated for the applied cuts and kinematics (see Figure 5.21 and 5.22). This provided values for these two coefficients (see Table 5.5). In terms of these mixing coefficients, the purity factor is then

$$D_n = \frac{N_n^n}{N_n^n + N_p^n} = \frac{\frac{\sigma_n}{\sigma_p}\frac{\nu_n^n}{\nu_p^p}}{\frac{Z_{tgt}}{N_{tgt}}\frac{\nu_p^n}{\nu_p^p} + \frac{\sigma_n}{\sigma_p}\frac{\nu_n^n}{\nu_p^p}} \ . \tag{5.18}$$

Using this information, it is possible to solve for the mixing ratios from the ratios of hydrogen (H_2), ^{3}He, and nitrogen (N_2)

$$\frac{\nu_p^n}{\nu_p^p} = R_H \ , \tag{5.19}$$

$$\frac{\nu_n^p}{\nu_p^p} = \frac{\sigma_p}{\sigma_n}\left[\frac{R_{He}\frac{Z_{He3}}{N_{He3}} - \frac{Z_N}{N_N}R_N + \left(\frac{Z_N}{N_N} - \frac{Z_{He3}}{N_{He3}}\right)R_H}{R_N - R_{He}}\right] \ , \tag{5.20}$$

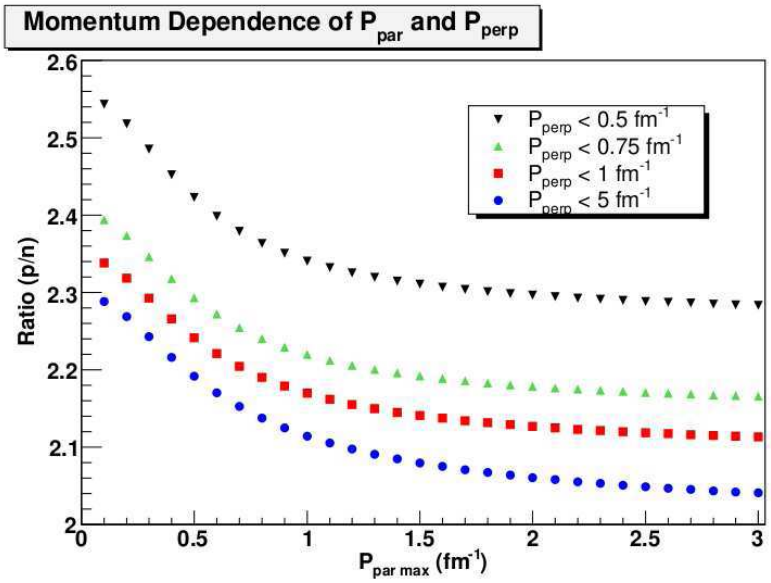

Figure 5.22: Presented is the ratio of protons to neutrons within the target for ^{3}He. Shown are from cuts on $p_\perp$. The applied cut on $p_\perp$ was 0.15 GeV with $P_\parallel$ cuts of 400, 250, and 200 MeV for kinematics of $Q^2 = 3.5$, 2.5, and 1.7 GeV^2. Shown is the ratio for various cuts of inverse distance. This study was done by Aidan Kelleher.

$$\frac{\nu_n^n}{\nu_p^p} = \frac{\sigma_p}{\sigma_n}\left[R_N\left(\frac{Z_{He3}}{N_{He3}} - \frac{Z_N}{N_N}\right)\frac{R_{He} - R_H}{R_N - R_{He}} - \frac{Z_N}{N_N}R_H\right] \quad . \tag{5.21}$$

Therefore the dilution due to the proton to neutron conversion in the sample,

$$D_n = \frac{R_{He}[(\frac{Z_{He3}}{N_{He3}} - \frac{Z_N}{N_N})R_N + \frac{Z_N}{N_N}R_H] - \frac{Z_{He3}}{N_{He3}}R_N R_H}{R_{He}\left(\frac{Z_{He3}}{N_{He3}} - \frac{Z_N}{N_N}\right)(R_N - R_H)} \quad . \tag{5.22}$$

This accounts for mixing due to conversions in the air and other material between the target and the veto detectors. However, there are additional considerations due to the veto detectors before the final dilution factor, due to protons observed as neutrons, can be determined.

As mentioned in section 5.4, the veto detector efficiency was related to large dead-time in the veto detector TDCs and high rate within the veto detectors. The dead-time could be as high as 110 ns for some paddles, while the rate in the indi-

vidual veto detectors was on the order of 1 MHz. Additionally, the hydrogen and nitrogen data were acquired at different rates than the ^{3}He data. Because of this, it is desirable to account for the rate dependence in the charge identification. This is complicated for a couple of different reasons. First, the veto was segmented into left and right and into two planes, which made the veto difficult to model. Also, because of the high activity in the veto, every event had multiple random hits within the veto planes.

The observed protons and neutrons detected in the veto can be represented in the following equations, where the $f_{p(n)}$ stands for the fraction of protons(neutrons) incident on the veto detectors over the total number of hadrons incident on the veto detectors; which is equivalent to the fraction when there is no deadtime. In these equations r represents the rate in the detectors.

$$N_n^p(r) + N_p^p(r) = f_p T(r) + f_n T(r) P_{busy}^{veto}(r) \tag{5.23}$$

$$N_n^n(r) + N_p^n(r) = f_n T(r)(1 - P_{busy}^{veto}(r)) \tag{5.24}$$

A charged hit is determined by a hit in the proper range of either veto plane (see Table 5.4). So the rate dependent number of observed neutrons is the rate dependent total number of hadrons, $T(r)$, incident on the neutron detector multiplied by the fraction, f_n, of the number of neutrons to hadrons multiplied by the probability that there was no accidental background hit in the veto detector to make it appear charged $(1 - P_{busy}^{veto})$. The rate dependent number of observed protons is the total number of hadrons multiplied by the fraction of protons over hadrons, f_p, plus

the fraction of neutrons misidentified by the accidental background.

These probabilities can be determined by modeling them using the Poisson distribution, and then adding up all the probabilities for each hadron event. This gives real numbers for everything but the fractions incident on the veto detectors. The observed ratios, at a given frequency, are

$$R_{tgt}(r) = \frac{N_n^n(r) + N_p^n(r)}{N_n^p(r) + N_p^p(r)} \ . \tag{5.25}$$

Using this formula twice, once for the observed rate r and once for the desired rate d, gives a formula to relate every observed ratio $R_{tgt}(r)$ to a desired ratio $R_{tgt}(d)$:

$$R_{tgt}(r) = \frac{R_{tgt}(d)T(d)[F^r(\beta)]}{R_{tgt}(d)T(d)[T(r) - F^r(\beta)] + [F^d(\beta) - R_{tgt}(d)(T(d) - F^d(\beta))]T(r)} \ . \tag{5.26}$$

The fitting parameter β accounts for correlations in hits in different veto bars in a given event. The function F depends on β and ξ, where ξ is the total rate dependent probability for veto detectors to be busy in an event:

$$F^r(\beta) = \sum_0^{T(r)} P_{busy}(\beta, r) \ . \tag{5.27}$$

here ξ is a useful quantity to define for the calculation and fit of

$$F^r(1) = \xi(r) = \sum_0^{T(r)} P_{busy}(\beta = 1, r) \ , \tag{5.28}$$

which is just $F^r(\beta)$ assuming no correlation between veto hits. The probability of an accidental hit, $P_{busy}(\beta)$ with r being the rate and τ being the dead-time (or busy time) of the bar, in a given event is

$$P_{busy}(\beta, r) = (e^{-\sum r\tau})^\beta \ . \tag{5.29}$$

The functional form of $F^r(\beta)$ can be approximated by assuming that the rate r multiplied by the deadtime τ_d is approximately the same for all bars, so the quantity $A = e^{-\sum r\tau_d}$ is the same for each bar. This is a good assumption, since the rate multiplied by dead-time is the same order of magnitude for all veto bars. From this,

$$F^r(1) = \xi(r) \approx T(r)A(r) \ . \tag{5.30}$$

Therefore a good approximation for $F(\xi, \beta)$ is

$$F^r(\beta) \approx T(r) \left(\frac{\xi(r)}{T(r)} \right)^{\beta} \ . \tag{5.31}$$

This allows the ratio at a specific rate of the different targets to be calculated using the fractions of uncharged and charged particles incident on the veto. Using these ratios in equation 5.22 gives the rate independent dilution correction for proton to neutron conversion:

$Q^2 =$	Ratio for ^{3}He	Ratio for Hydrogen	Ratio for Nitrogen	Purity Factor
2.5 GeV^2	0.102 ± 0.001	0.019 ± 0.002	0.193 ± 0.010	0.8 ± 0.03
3.5 GeV^2	0.073 ± 0.001	0.014 ± 0.002	0.107 ± 0.053	0.865 ± 0.053
1.7 GeV^2	-	-	-	-

Table 5.3: A table of the ratios for different criteria. Over the course of a kinematic setting, runs varied in rate. This had a small effect on the purity factor, the results presented in this table is for a normal run.

name	Helium Ratio	Nitrogen Ratio
Kin 2	2.15	1.07
Kin 3	2.31	1.07
Kin 4	2.15	1.07

Table 5.4: The effective ratio of $\frac{Z}{N}$ for the target and cuts.

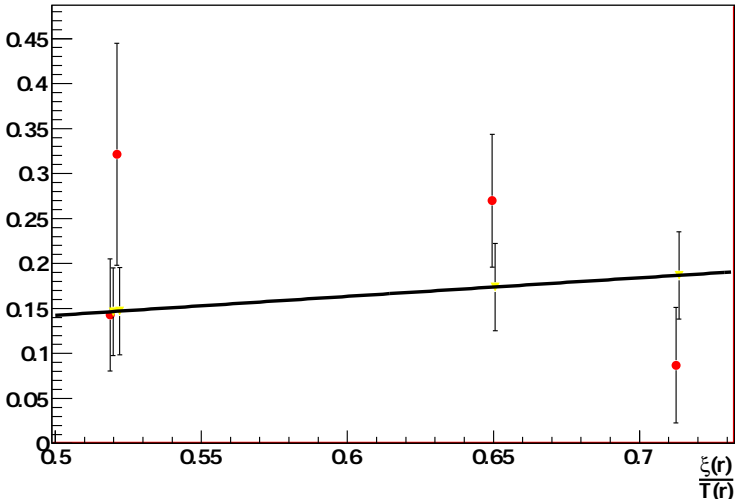

(a) uncharged to charged ratio for $Q^2 = 2.5$ GeV^2

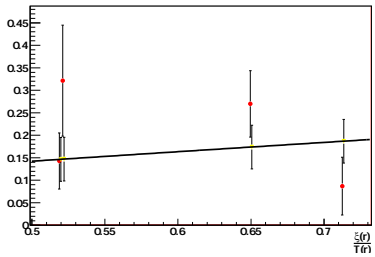

(b) uncharged to charged ratio for $Q^2 = 3.5$ GeV^2

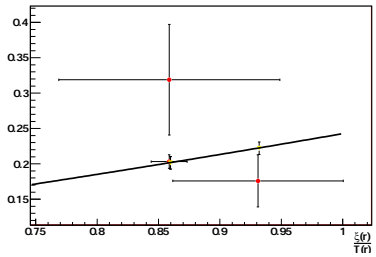

(c) uncharged to charged ratio for $Q^2 = 1.7$ GeV^2

Figure 5.23: Shown in these figures is the measured uncharged to charged ratio, the uncharged to charged ratio within the model, and the fit line of the model in nitrogen. These are plotted against the natural dependence $\frac{\xi}{T}$.

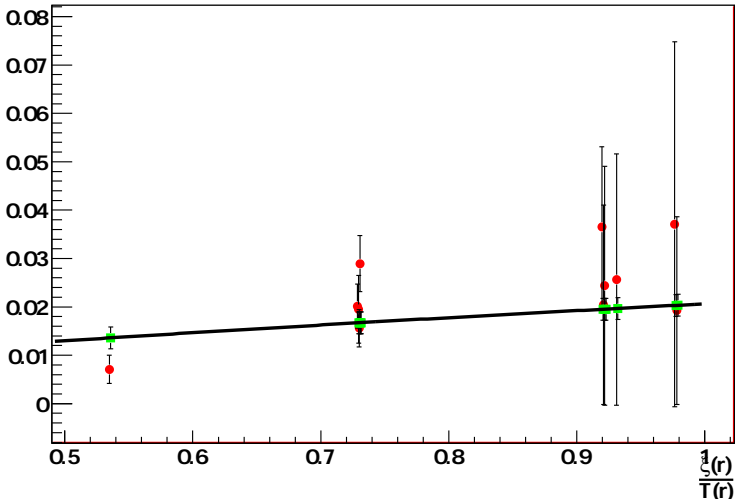

(a) uncharged to charged ratio for $Q^2 = 2.5$ GeV^2

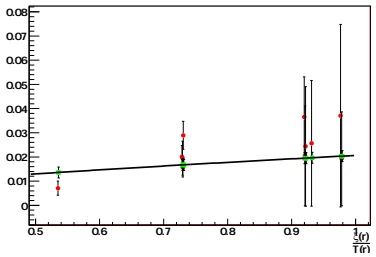

(b) uncharged to charged ratio for $Q^2 = 3.5$ GeV^2

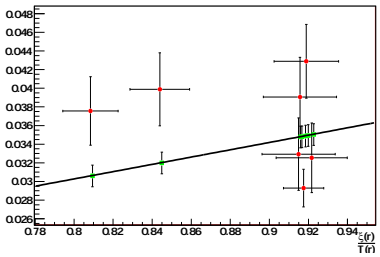

(c) uncharged to charged ratio for $Q^2 = 1.7$ GeV^2

Figure 5.24: Shown in these figures is the measured uncharged to charged ratio, the uncharged to charged ratio within the model, and the fit line of the model in hydrogen. These are plotted against the natural dependence $\frac{\xi}{T}$.

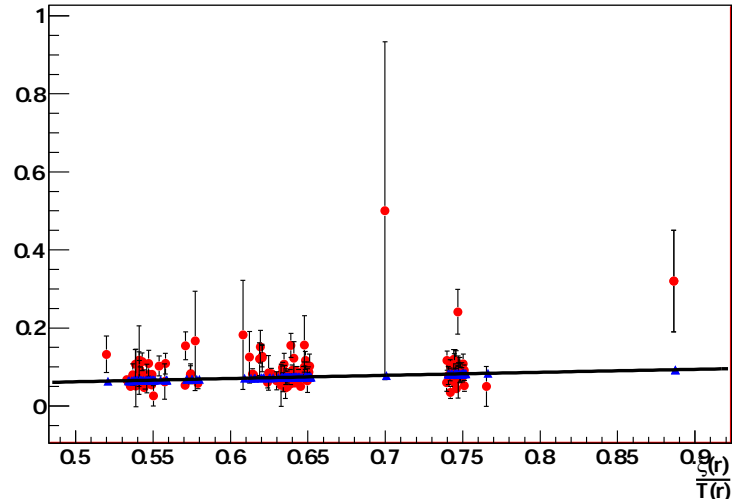

(a) uncharged to charged ratio for $Q^2 = 2.5$ GeV^2

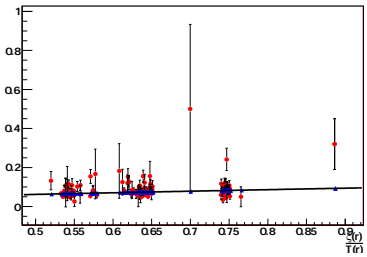

(b) uncharged to charged ratio for $Q^2 = 3.5$ GeV^2

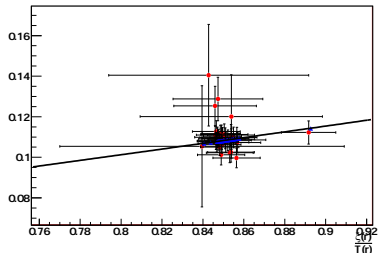

(c) uncharged to charged ratio for $Q^2 = 1.7$ GeV^2

Figure 5.25: Shown in these figures is the measured uncharged to charged ratio, the uncharged to charged ratio within the model, and the fit line of the model in ^{3}He. These are plotted against the natural dependence $\frac{\xi}{T}$.

$$D_n = \frac{R_{He}(d)[(\frac{Z_{He3}}{N_{He3}} - \frac{Z_N}{N_N})R_N(d) + \frac{Z_N}{N_N}R_H(d)] - \frac{Z_{He3}}{N_{He3}}R_N(d)R_H(d)}{R_{He}(d)\left(\frac{Z_{He3}}{N_{He3}} - \frac{Z_N}{N_N}\right)(R_N(d) - R_H(d))} \ . \qquad (5.32)$$

5.5.1 Single Track Analysis and Background Correction

For approximately 10% of the detected events, the hadron interacted in the lead resulting in multiple events in the neutron apparatus or an accidental background hit that could not be differentiated from the hadron. If there were two or more hits in the region of parameter space used to select quasi-elastic events (hereafter known as the quasi-elastic region), the charge becomes impossible to determine since just one "hit" in the veto detectors associated with the quasi-elastic region will often set all hits in the quasi-elastic region as charged.

By restricting the analysis to only those events which have a single hit identified as quasi-elastic, the problem of charge identity and multiple hits in the quasi-elastic region is solved. Using this single track analysis (SQE), however, causes the determination of the background to become more complicated.

When multi-hit events are eliminated, the spectrum far from the quasi-elastic hit is clean (see Figure 5.29). Using the perpendicular transferred momentum, $q_\perp$, the distance far from the quasi-elastic hit can be parametrized in the same variable which is used to select quasi-elastic events. In this band of $q_\perp$, the ratio of charged to uncharged background is relatively constant (see Figure 5.28). This gives the ratio of charged to uncharged for the background which is unrelated to the quasi-elastic events. The only determination that is made in this region is the charge ratio of the

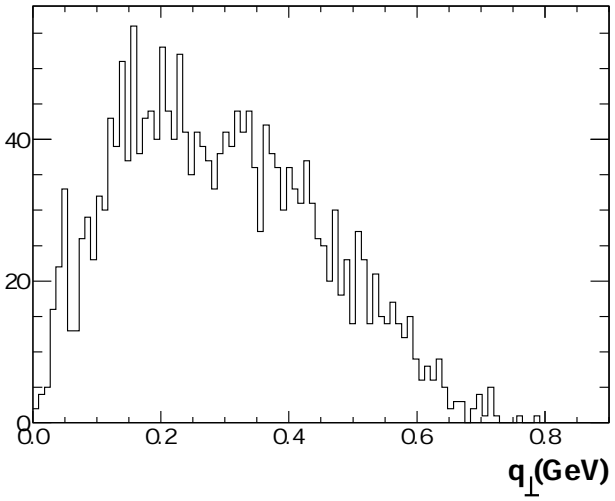

Figure 5.26: Plot $q_\perp$ for a region in time. This is 5 ns removed from the peak region.

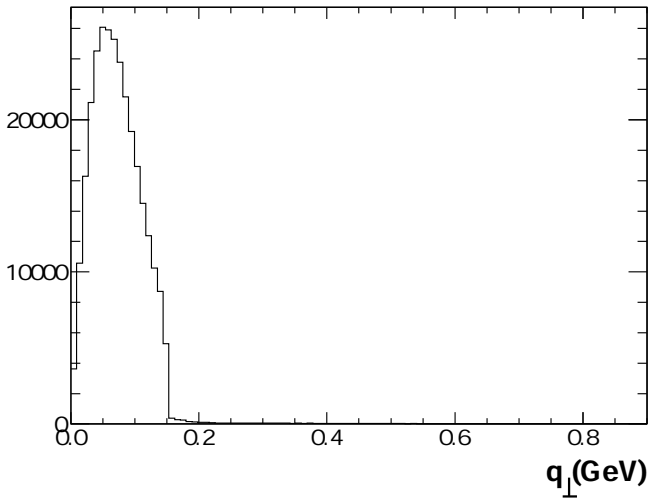

Figure 5.27: Plot $q_\perp$ for a region in time. This is at the quasi-elastic region.

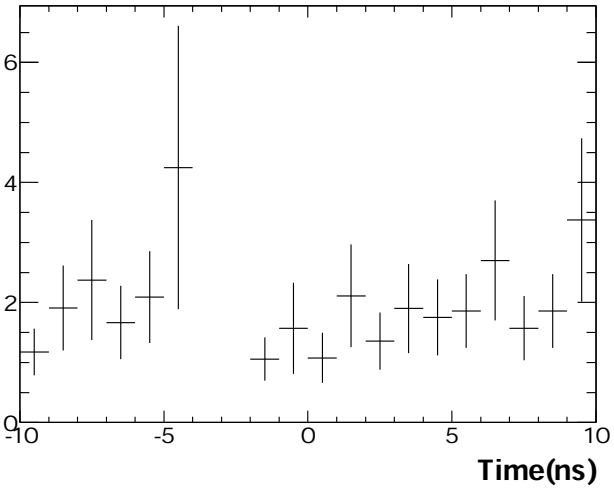

Figure 5.28: Plot of the ratio of uncharged to charged for the region of $q_\perp$ between 0.55 and 0.60 GeV/c. The region near 3 ns is removed due to the photon peak being there. Add axis information time (ns), update description (changed plot)

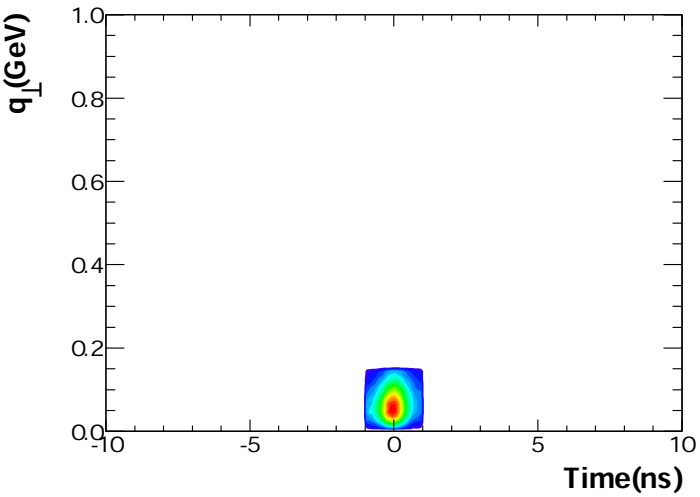

Figure 5.29: Plot of $q_\perp$ versus time-of-flight for events with only a single hit in the $|t| < 7$ and $q_\perp < 0.15$ region. The area in the spectrum of events coming from k photons via π_0 production was removed (between 2 and 4 ns). This is for runs 4090-4099.

background. The total background count is determined via a different mechanism.

Since it is required that every hit in the quasi-elastic region is either a single quasi-elastic hit, or a single background hit, the total number of counts (and events) is:

$$N_{SQE}^{A+B} = N_{back}^{A} + N_{QE}^{A} + N_{back}^{B} + N_{QE}^{B} \ , \tag{5.33}$$

where A and B are two regions within the SQE region. The SQE region is chosen so as to include all of the quasi-elastic events within it. It is useful to define region B as being a region where $N_{QE}^{B} = 0$.

This is a lot simpler than that of the full events, which can be expressed as the following:

$$N_{full}^{A+B} = N_{back}^{A} + N_{QE}^{A} + N_{QE}^{A}|_{back} + N_{back}^{A}|_{back} + N_{back}^{B}|_{back} + N_{QE}^{B}|_{back} + N_{QE}^{A}|_{QE} + N_{back}^{A}|_{QE} + N_{back}^{B} + N_{back}^{B}|_{QE} \ ,$$

here $|_{back}$ is the number of hits which also have at least one background hit, $|_{QE}$ is the number of hits with at least one QE hit. Another class of hits are $N_{QE}^{A}|_{QE}$ which are the number of QE hits with at least one other QE hit; these would be from fragmentation caused by interaction between the target and the final hit location in the neutron arm. Here A is the SQE region with the quasi-elastic hits within it and B is a region in the SQE region without any quasi-elastic hits.

If the region is restricted to being outside the QE region, the expression is left as:

$$N_{full}^{B} = N_{back}^{B} + N_{back}^{B}|_{back} + N_{back}^{B}|_{QE} \ . \tag{5.34}$$

Obviously it is just desired to remove the N_{back}^{B} from the QE sample in region A.

Since equation 5.33 is true for SQE analysis, outside of the QE region the expression for the counts is

$$N^B_{SQE} = N^B_{back} \ , \tag{5.35}$$

due to $N^B_{back}|_{back}$ and $N^B_{back}|_{QE}$ events not occuring because only one hit can occur in the SQE region. Once the regions A and B are scaled to be the same size, the number of quasi-elastic events in SQE analysis can be determined

$$N_{QE} = N_{A,SQE} - N_{B,SQE} \ , \tag{5.36}$$

here B is a sub region of the SQE region where the QE events don't reside, and A is the sub region of the SQE region where QE events do reside.

For times earlier than the quasi-elastic window, as described above the hits are all background, coming from an accidental coincidence between the electron and hadron (see Figure 5.29). This is in the -4 ns to -7 (or -13) ns window. Using the counts (scaled properly) from this background region provides the background in single quasi-elastic hit analysis. The same area in $q_\perp$ is used to make scaling easier. To determine the neutral accidental background, the earlier determined background ratio term is used:

$$N_{neut,back} = N_{back} f_{back} \ , \tag{5.37}$$

here f is the fraction of neutrals to hadrons in the background.

These background counts, neutral or charged, are used to determine the accidental background dilution and asymmetry used in the determination of the physical asymmetry. The neutral background dilution of a sample (N) can be expressed as

$$D_{back} = 1 - \frac{N_{neut,back}}{N} \ . \tag{5.38}$$

Similarly the background asymmetry can be defined in the standard way

$$A_{back} = \frac{N^{+}_{back} - N^{-}_{back}}{P_{^3He} N} \ . \tag{5.39}$$

5.5.2 Nitrogen Dilution

The ^{3}He inside the target cell is diluted by unpolarized nitrogen, used as a buffer gas to decrease interactions between the polarized ^{3}He and glass cell walls and to aid in the polarization process (Section 4.4.2). This contamination creates a dilution of the ^{3}He asymmetry, and is measured by looking at events which appear to be quasi-elastic in a N_2 target and scaling by the relative densities and total charge on target. This dilution factor is

$$D_{N_2} = 1 - \frac{N_{N_2} - N_{back,N_2}}{N - N_{back}} \frac{Q_{^3He} \rho_{^3He}}{Q_{N_2} \rho_{N_2}} \ . \tag{5.40}$$

The values used to calculate this dilution factor are provided in Table 5.5. Quasi-elastic event selection, discussed earlier in the chapter, was used to select the events used for this analysis.

ρ_{QE}	Q^2	ρ_{N_2}	$Q_{^3He}$	Q_{N_2}	D_{N_2}	N	N_{back}	N_{N_2}	N_{back,N_2}
0.162	2.5	4.4	18399	14020	0.949	2089.1	46.2	220.5	14.9
0.162	3.5	3.6	1441010	37920	0.982	2686.2	52.6	28.5	5.5
99	1.7	99	99	99	99	99	99	99	99

Table 5.5: A table for the Nitrogen Dilution factor determination. Uncertainties are discussed in Appendix B. Densities are determined from measurements of the target [51][46][68].

5.5.3 RF correction

While the timing of the coincidence event relative to the beam crossing cannot be determined absolutely, it can be determined up to an arbitrary constant. Event by event variations about this constant can be determined from the 499 MHz RF signal, which can be used to improve the hadron time-of-flight measurement between the target and detectors.

The signal from the RF is put into the F1 TDC, which wraps (starts counting again at 0) at $W = 65526$ channels, and has $t_{res} = 0.1183$ ns resolution. The RF signal repeats in a $T_{win} = 2$ ns window. In the following formula t_{RF} = RF time, t_{ref} = reference time, t_{L1A} = level 1 accept time, and the aforementioned time-of-flight (equation 5.9).

The RF correction is calculated using the following formula

$$RF_{corr} = \frac{V_{tgt}}{c} + t_{res}\left(t_{RF} - t_{ref} - \left(\left[\frac{t_{RF} - t_{ref}}{0.5W}\right] \textbf{ mod } 1\right)W\right) , \tag{5.41}$$

$$t_{rf} = \left[(t_e - t_{L1A} - RF_{corr} - t_{rfshift}) \textbf{ mod } \left(\frac{1}{0.499}\right) + \frac{2}{0.499}\right] \textbf{ mod } \left(\frac{1}{0.499}\right) . \tag{5.42}$$

This t_{rf} is the shift used for correcting the time-of-flight in equation 5.9. The $t_{rfshift}$ is the peak location shown in Figure 5.30. This shift is plotted versus run number in Figure **??**. This correction is due time of the scattering within the target.

5.6 Asymmetry calculation

After the selection of quasi-elastic neutron events (Table 5.6), the measured asymmetry is corrected to give the physical asymmetry, which gives G_E^n as presented

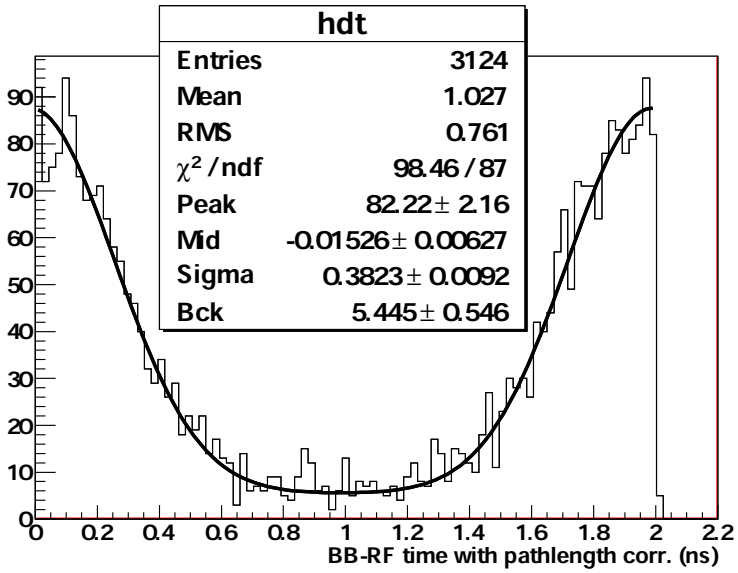

Figure 5.30: Spectrum used to determine the RF correction. This is for run 3888. The peak location is determined from the Mid parameter, which is $t_{rfshift}$.

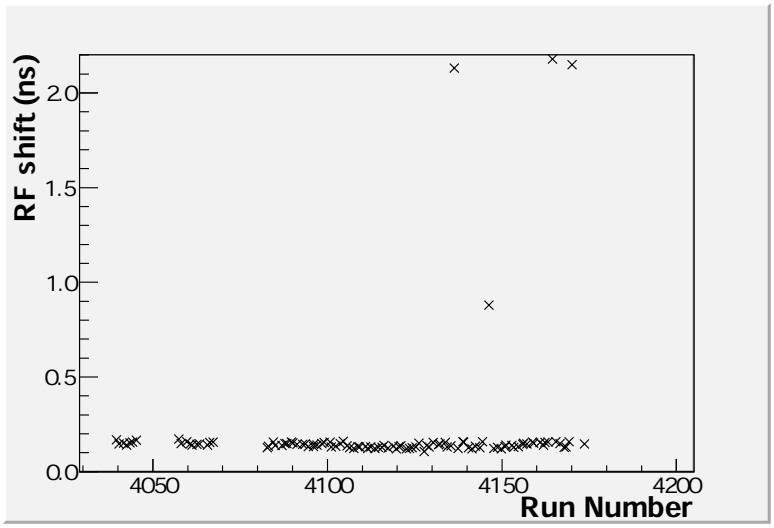

Figure 5.31: RF correction versus run number for $Q^2 = 2.5$ GeV^2. Note that since the plotted function is **mod** $\left(\frac{1}{0.499}\right)$ that the values of 2 ns and 0 ns are almost equivilent.

Name	$Q^2 = 2.5$ GeV^2	$Q^2 = 3.5$ GeV^2	$Q^2 = 1.7$ GeV^2
Time (ns)	$\|t\| < 2$	$\|t\| < 1$	$\|t\| < 1$
Invariant Mass (GeV)	$\|w - 0.9\| < 0.2$	$\|w - 0.775\| < 0.175$	$\|w - 0.9\| < 0.2$
Q Perp (GeV)	$q_\perp < 0.15$	$q_\perp < 0.15$	$q_\perp < 0.15$
SQE region B	$\|t - 8.5\| < 4.5$	$\|t - 8.5\| < 4.5$	$\|t - 8.5\| < 4.5$
Missing Mass (GeV)	$M_{miss} < 2$	$M_{miss} < 2$	$M_{miss} < 2$
Vertical Cut (m)	$\|X + 0.2\| < 1.7$	$\|X + 0.2\| < 1.7$	$\|X + 0.2\| < 1.7$
Horizontal Cut (m)	$\|Y + 0.183\| < 0.7$	$\|Y + 0.183\| < 0.7$	$\|Y + 0.183\| < 0.7$

Table 5.6: Table of quasi-elastic event selection cuts. The Single QE cut is that there is one and only one hit in the associated region of time and $q_\perp < 0.15$. This is in addition to the region of time and $q_\perp$ which are selected as quasi-elastic event candidates. The vertical cut and horizontal cut are neutron arm fidicual cuts.

in section 3.3.3. This is the general expression, as mentioned in the previous sections there are corrections which need to be done for nitrogen dilution in the target cell (section 5.5.2), proton to neutron coversion between the target and scintillator bars (section 5.5), accidental background asymmetry and dilution (section 5.5.1), neutron polarization in the nucleus [32], beam polarization (section 4.3), target polarization (section 4.4), and final state interactions (section 5.7.1). The corrected expression is

$$A_{Phys} = \frac{A_{sum} - A_{proton} - A_{back}}{P_{^3He} P_{beam} P_n D_{N_2} D_n D_{FSI} D_{back}} \ . \tag{5.43}$$

Since the proton contamination of the neutron sample (D_n), proton asymmetry (A_{proton}), nitrogen dilution (D_{N_2}) , background asymmetry (A_{back}), and background dilution (D_{back}) all depend on similar quantities, corrections need to be applied as presented in sections 5.7 and 5.5. The nitrogen dilution is corrected for the background dilution and the proton contamination dilution is corrected for both the nitrogen dilution and the background dilution.

The physical asymmetry, corrected for the discussed dilutions and asymme-

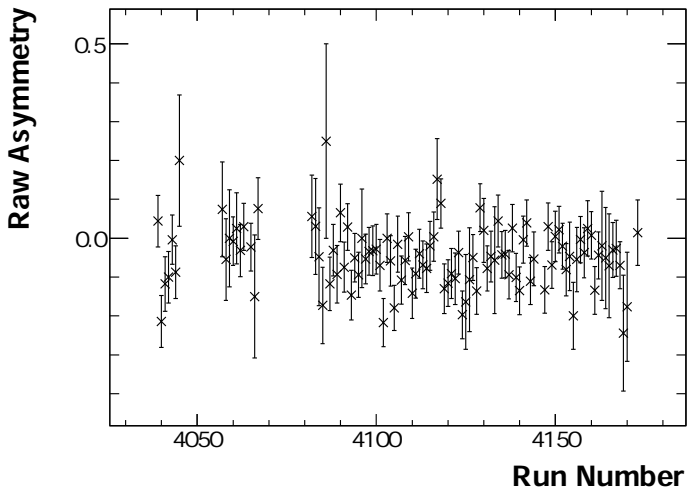

Figure 5.32: Shown is the run number versus raw asymmetry for $Q^2 = 2.5$ GeV^2.

tries, is presented in Table 5.7. The dilutions can be expressed in terms of those due to polarization (P), those due to theoretical calculations like FSI (D_{fsi}) and neutron polarization (P_n), and experimental corrections not due to polarization (V). Expressed this way

$$P = P_{^3He} P_{beam} \tag{5.44}$$

and

$$V = D_n D_{N_2} D_{back} \ . \tag{5.45}$$

At times during the measurements at $Q^2 = 2.5$ and 3.5 GeV^2, the target cell and beam were changed. This meant that the P_{beam}, $P_{^3He}$, and D_n could change during the run. To account for this, the target polarization corrected the asymmetry on a run by run basis. Using standard error analysis (and Appendix B), the summation was

$$A_{sum} = \frac{\sum A_i \frac{1}{\sigma_i^2}}{\sum \frac{1}{\sigma_i^2}} \ , \tag{5.46}$$

$Q^2 =$	1.7 GeV^2	2.5 GeV^2	3.5 GeV^2
A_{meas}	-0.0437 ± 0.0096	-0.0449 ± 0.0055	-0.0356 ± 0.0081
N	10882	3301	15381
P_{nucl}	0.4928 ± 0.02	$0.436 \pm (0.02)$	$0.477 \pm (0.02)$
P_{beam}	$0.835 \pm (0.03)$	$0.835 \pm (0.03)$	$0.835 \pm (0.03)$
P_n	$0.86 \pm (0.02)$	$0.86 \pm (0.02)$	$0.86 \pm (0.02)$
D_{back}	0.994	0.9792 ± 0.0003	0.9732 ± 0.0005
A_{back}	0.0002 ± 0.03	0.0013 ± 0.0001	0.0013 ± 0.00003
D_n	0.823 ± 0.033	$0.8 \pm 0.023 \pm (0.04)$	$0.865 \pm 0.046 \pm (0.043)$
A_{proton}	-0.0003 ± 0.0001	-0.00089 ± 0.0002	-0.0006 ± 0.0001
D_{N_2}	0.946 ± 0.001	$0.949 \pm 0.004 \pm (0.005)$	$0.982 \pm 0.004 \pm (0.002)$
P	-	0.364	0.398
V	-	0.744	0.826
A_{phys}	-0.190 ± 0.040	$-0.198 \pm 0.024 \pm (0.022)$	$-0.130 \pm 0.031 \pm (0.014)$

Table 5.7: Determination of the physical asymmetry from the measured experimental asymmetry. A full discussion and analysis of errors is presented in Appendix B.

$$\sigma_{sum} = \frac{1}{\sqrt{\sum \frac{1}{\sigma_i^2}}} \ , \tag{5.47}$$

where the above equation was used for statistical uncertainties and the A_i are the measured asymmetries for each run. After this summation, the physical asymmetry is calculated using

$$A_{Phys} = \frac{A_{sum} - A_{proton} - A_{back}}{P_{beam} P_n D_{N_2} D_n D_{FSI} D_{back}} \ . \tag{5.48}$$

Many runs were taken over the course of a measurement at a given Q^2. The stability of the asymmetry over the course of the run, for a given running condition, was stable as shown in Figure 5.32.

While the other asymmetries and dilutions can be corrected for without using acceptance information, the FSI dilution and proton asymmetry require knowledge of the kinematics to be properly applied.

The framework using knowledge of the kinematics to determine the ratio of

the electric and magnetic form factors, and so determine G_E^n, is based on equation 3.15. This provides the relationship between kinematic variables, the asymmetry, and the form factor ratio. The relation between the physical asymmetry and the ratio, λ, can be expressed as:

$$A = \frac{B\lambda + C}{\lambda^2 + D} \ , \tag{5.49}$$

where $\lambda = \frac{G_E}{G_M}$ is the form factor ratio, and B, C, and D are the following kinematic quantities

$$B = -2\sqrt{\tau(1+\tau)}\tan(\frac{\theta_e}{2})\sin\theta\cos\phi \ , \tag{5.50}$$

$$C = -2\tau\sqrt{1+\tau+(1+\tau)^2\tan^2(\frac{\theta_e}{2})}\tan(\theta_e)\cos\theta \ , \tag{5.51}$$

$$D = -\tau + 2\tau(1+\tau)\tan^2(\frac{\theta_e}{2}) \ . \tag{5.52}$$

and the quantities τ, θ_e, θ, and ϕ were defined in section 4.4.2. These quantities can be averaged from all events, and are used in the determination of the proton asymmetry correction, the determination of Q^2, and the determination of λ from the physical asymmetry.

The dilution corrections are presented explicitly in section 5.5. The asymmetry corrections will be presented explicitly here. To make the best use of the good proton form factor measurements [63], values for the proton form factor ratio were used to determine the A_{proton}. The equations 5.50, 5.51, and 5.52 were used to calculate the proton physical asymmetry

$$A_{phys,proton} = \frac{(B\lambda_{proton} + C)}{\lambda_{proton}^2 + D} \ . \tag{5.53}$$

This can then be corrected for the nitrogen dilution of the charged events (D_{ch,N_2}), the proton polarization (P_p), background dilution (D_{back}), and the beam polarization

(P_{beam}) to give the proton asymmetry correction

$$A_{proton} = \frac{1 - D_N}{D_{back} D_{N_2}} P_{beam} P_p A_{phys,proton} \ . \tag{5.54}$$

By using the plot of this ratio at different values of the physical asymmetry, the error and value for the ratio can be determined. However, if instead of being plotted, λ is solved for, an inversion must be used. This can be done using the following method [31]. Using equation 5.50, 5.51 and 5.52, we can express 5.49 as:

$$\frac{\Delta(\theta,\phi)}{\Sigma(\theta,\phi)} = A_{phys} = \frac{B\lambda + C}{D + \lambda^2} = \frac{C}{D} + \frac{B}{D}\lambda - \frac{C}{D^2}\lambda^2 - \frac{B}{D^2}\lambda^3 + \frac{C}{D^3}\lambda^4 + \frac{B}{D^3}\lambda^5 \ . \tag{5.55}$$

$Q^2 =$	1.7 GeV^2	2.5 GeV^2	3.5 GeV^2
A_{phys}	-0.190 ± 0.040	$-0.198 \pm 0.024 \pm 0.022$	$-0.130 \pm 0.031 \pm 0.014$
T0	-0.0156	-0.0128	-0.0752
T1	0.8362	0.8353	0.9844
T2	0.0134	0.0114	0.0927
T3	-0.6832	-0.6811	-1.1977
T4	-0.0116	-0.0102	-0.1159
T5	0.5660	0.5640	1.4805
λ	-0.218 ± 0.054	$-0.232 \pm 0.033 \pm 0.031$	$-0.250 \pm 0.047 \pm 0.021$

Table 5.8: Expansion Coefficients in the determination of λ from the physical asymmetry. Uncertainty in λ calculated as discussed in Appendix B.

These expansion coefficients can be expressed as $T_0 = \frac{C}{D}$, $T_1 = \frac{B}{D}$, $T_2 = \frac{C}{D^2}$, $T_3 = \frac{B}{D^2}$, $T_4 = \frac{C}{D^3}$, and $T_5 = \frac{B}{D^3}$. In this expansion, these provide all the acceptance and kinematic information for a given event. This allows the expression of A_{phys} as a polynomial in λ with coefficients being equal to the averaged T_n values. For specific averaged values, λ can be solved for giving the ratio of the electric and magnetic form factors for that specific kinematic. To first order, this lambda is

$$\lambda_0 = \frac{A_{phys} - \langle T_0 \rangle}{\langle T_1 \rangle} \ . \tag{5.56}$$

Using these terms, the value for Q^2 was also corrected for finite acceptance:

$$Q^2 = \frac{\sum T_{1,i} Q_i^2}{T_1} \ . \tag{5.57}$$

The value for λ,

$$\lambda = \frac{G_E^n}{G_M^n} \ , \tag{5.58}$$

provides the electric form factor of the neutron as a ratio of the magnetic form factor. Using this corrected value for Q^2 and using the value of the magnetic form factor as determined from a common parameterization [48], the value of the electric form factor was determined. This calculation is presented in Table 5.9. The calculation of the uncertainty is presented in appendix B.

The results and discussion of them in relation to previous measurements and selected models are presented in Chapter 6.

$Q^2 =$	1.7 GeV^2	2.5 GeV^2	3.5 GeV^2
λ	$-0.218 \pm 0.054(0.030)$	$-0.232 \pm 0.033 \pm 0.031$	$-0.250pm0.047 \pm 0.021$
Q^2	1.75 (GeV^2)	2.49 (GeV^2)	3.48 (GeV^2)
G_M^n	-0.096 ± 0.005	-0.0955 ± 0.0018	-0.0557 ± 0.0011
G_E^n	$0.021 \pm 0.005(0.003)$	$0.0221 \pm 0.0032 \pm 0.0030$	$0.0139 \pm 0.0026 \pm 0.0012$

Table 5.9: Displayed is the calculated values for λ and Q^2, and the value of G_M^n as arrived at from a parameterization [48]. From this the value of G_E^n can be determined. Determination of uncertainty is discussed in Appendix B.

5.7 Corrections

5.7.1 FSI Corrections

As mentioned previously, in section 3.5, to first order there are four types of interactions at lower momentum transfer. Shown in Figure 5.33, these are the

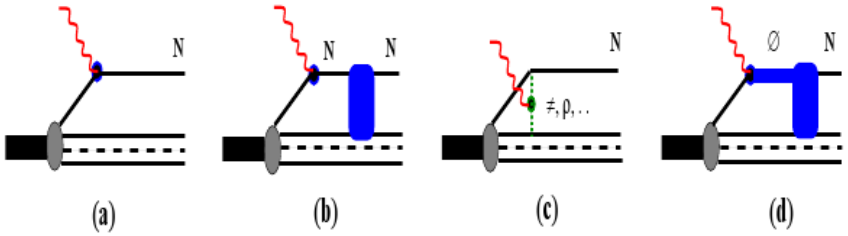

Figure 5.33: The four dominant lowest order diagrams in single nucleon scattering. Shown is (a) impulse approximation, (b) meson exchange currents, (c) isobar contributions, and (d) FSI. [75]

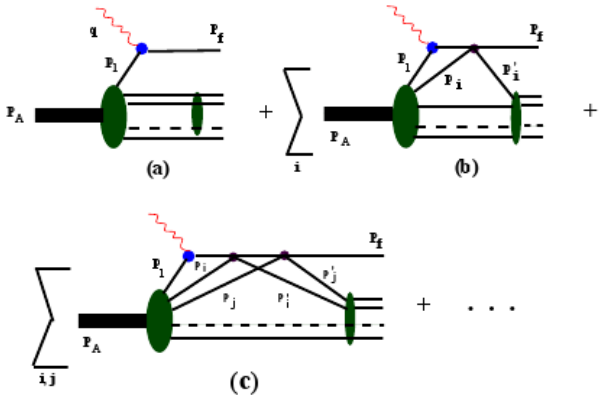

Figure 5.34: In nuclei with more than a single nucleon, the plane wave impulse approximation can be used to give the description of the interaction. Shown are the leading order diagrams for ^{3}He which is the PWIA diagram, single re-scattering diagram, and double re-scattering diagram. [75]

impulse approximation (IA), isobar current (IC), meson exchange currents (MEC), and final state interactions (FSI). As has already been argued, meson exchange currents and isobar currents are small for $Q^2 > 1$ GeV^2. This is due to them scaling as $\frac{1}{Q^4}$. This leaves just final state interactions as a necessary correction to the physical asymmetry, which was arrived at from the impulse approximation. The final state interactions are basedon on nucleon-nucleon cross sections, which are flat above 2 GeV [75]. To lowest order, these FSI will be either single or double re-scattering between the spectrator hadrons and the detected hadron (see Figure 5.34).

There are two similar approximations made in computing the effects of these FSI. These are the glauber approximation and the generalized eikonal approximation (GEA). In the glauber approximation the incident particles energy is assumed to be much larger than that of the potential, and is large enough so that the wavelength of the incident particle is smaller than the potential width. This means that the Glauber approximation truncates the terms after double scattering due to the spectator hadrons being considered at rest. In the generalized eikonal approximation, the high momentum particle can not interact with a slow hadron a second time after interacting with another bound hadron.

The eikonal approximation reduces to the Glauber approximation in the limit of zero longitudinal momentum transfer, $\Delta = \frac{q_0}{|q|}(E_s - m) \rightarrow 0$. Here q is transfered momentum, the subscript s refers to spectator, and m is the recoiling nucleon mass. This is due to the Glauber approximation assuming that all nucleons are stationary while the GEA allows for nonzero initial momentum of the recoiling nucleon [75].

5.7.2 Inelastic Contribution

The inelastic contribution to the quasi-elastic asymmetry is the final correction to be developed. This contribution can be limited by removing some of the quasi-elastic region which is closest to the delta resonance (at $W = 1.4$ GeV). The observed width of the quasi-elastic peak in the invariant mass spectrum is increased due to the motion of the nucleon within ^{3}He and due to the resolution of the detectors. The inelastic resonance width is similarly increased. This inelastic contribution increases the tail in the quasi-elastic sample towards greater invariant mass as demonstrated in Figures 5.10(a), 5.9(a), 5.8(a), and **??** for $Q^2 = 2.5$ GeV^2.

The inelastic contribution will be deconvoluted using a Monte Carlo (MC). This Monte Carlo is described in section A.2 and simulates the quasi-elastic and inelastic spectrum near the quasi-elastic spectrum. Using the inelastic counts under the quasi-elastic peak and the inelastic asymmetry from the simulation, the measured quasi-elastic asymmetry can have the contribution from inelastic events removed [69]. This Monte Carlo is being analyzed by another collaborator. When this is completed, the invariant mass cuts in Table 5.6 can be widened to 1.2 GeV.

The contribution of the inelastic sample can be emperically estimated by considering the asymmetry as a function of invariant mass. This shows the asymmetry both in the inelastic region, the quasi-elastic region, and the region with a significant inelastic contribution to the quasi-elastic events. This is demostrated in Figure 5.35.

Preliminary values for the inelastic asymmetry contribution and dilution are presented Table 5.10. The presented values are calculated in the framework of a

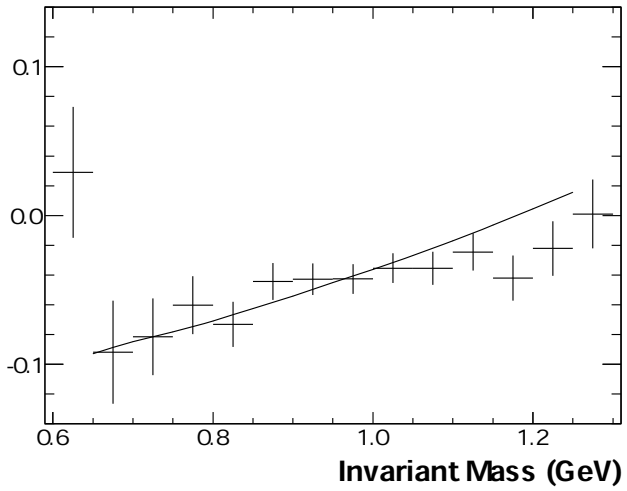

Figure 5.35: The asymmetry as a function of invariant mass. This shows that the invariant mass doesn't over the region selected (see Table 5.6).

seperate analysis with a different set of cuts and charge selection [68]. These are not included in the presented analysis here, but give an estimation to the contribution in the quasi-elastic event sample. The correction to the physical asymmetry due to the inelastic asymmetry and dilution is

$$A_{corr} = \frac{A_{phys} - A_{inelas}}{D_{inelas}} \ . \tag{5.59}$$

Q^2	D_{inelas}	A_{inelas}	A_{phys}
1.7 GeV^2	0.9839	-0.0038	-0.271
2.5 GeV^2	0.9834	-0.0030	-0.190
3.5 GeV^2	0.9726	-0.0050	-0.159
3.5 GeV^2*	0.905	-0.0143	-

Table 5.10: Shown are preliminary inelastic asymmetries and dilutions for the various kinematic [69]. The * row relates to an expanded selection of quasi-elastic events, with a maximum invariant mass of 1.2 GeV rather than the usual maximum of 1.05 (see Table 5.6).

As seen, with the cuts presented in Table 5.6 the contribution of the inelastic

events is small. The likliest source of a change in the results presented in Table 5.9 is due to increased theoretical understanding of ^{3}He nucleus. The results presented and discussed in Chapter 6 will be based off the results presented in Table 5.9.